

Mathematical morphology on the sphere: Application to Polarimetric Image processing

Joana Maria Frontera Pons

e-mail: joana.m.frontera@gmail.com

Centre de morphologie mathématique, École des Mines de Paris
Telecom BCN, Universitat Politècnica de Catalunya (UPC)



Escola Tècnica Superior d'Enginyeria
de Telecomunicació de Barcelona

UNIVERSITAT POLITÈCNICA DE CATALUNYA

Advisor: Dr. Jesús Angulo
e-mail: jesus.angulo@ensmp.fr

Fontainebleau, June 2011

Acknowledgements

First and foremost, I would like to thank my advisor, Jesús Angulo, for encouraging me and being an invaluable guide through my first experience in the world of research.

Thanks to my friends and colleagues for its support in the distance.

Finally, thanks so much to my family and all those who have made possible I spent these months in Paris.

Abstract

Title: Mathematical morphology on the sphere: Application to Polarimetric Image processing

Author: Joana Maria Frontera Pons

Department: Centre de morphologie mathématique

Advisor: Dr. Jesús Angulo

Abstract:

The fully polarimetric synthetic aperture radar (PolSAR) provides data containing the complete scattering information. Therefore, these data have drawn more attention in recent years. PolSAR data can be represented as polarization states on a sphere. We present image processing techniques based on the analysis of the polarimetric information within its location on the sphere.

Mathematical morphology is a well-known nonlinear approach for image processing. It is based on the computation of minimum and maximum values of local neighborhoods. That necessitates the existence of an ordering relationship between the points to be treated. The lack of a natural ordering on the sphere presents an inherent problem when defining morphological operators extended to unit sphere. We analyze in this project some proposals to the problem of ordering on the unit sphere, leading to formulations of morphological operators suited to the configuration of the data. The notion of local supremum and infimum is introduced, which allows to define the dilation and erosion on the sphere. Supervised orderings are considered and its associated operators for target recognition issues. We also present various filtering procedures for denoising purposes. The different methods studied in this project pursuit the generalization of the morphological operators on the sphere. Through the analysis performed, we pretend to achieve an understanding of the data and automation of the target detection.

Keywords: Image processing, Mathematical morphology, Sphere, SAR Processing, Polarimetry

Résumé

Titre: Morphologie mathématique sur la sphère: Application à le traitement des Images Polarimetrics

Auteur: Joana Maria Frontera Pons

Département : Centre de morphologie mathématique

Advisor: Dr. Jesús Angulo

Résumé

Le radar à ouverture synthétique polarimétrique (PolSAR) fournit des données polarimétriques, qui restituent la totalité de l'information portée par les ondes recueillies. Ces données, qui peuvent être représentées comme des états de polarisation sur une sphère, ont fait l'objet de nombreuses recherches au cours des dernières années. Nous nous intéressons dans le cadre de ce mémoire à des techniques de traitement d'image basées sur l'analyse de l'information polarimétrique directement sur la sphère.

La morphologie mathématique offre une approche non-linéaire éprouvée dans le domaine du traitement d'image. Cette théorie est basée sur le calcul de valeurs minimales et maximales dans des voisinages locaux, ce qui nécessite l'existence d'une relation d'ordre entre les points à traiter. L'absence d'une relation d'ordre naturelle sur la sphère constitue donc un problème délicat si l'on souhaite étendre la définition des divers opérateurs morphologiques au cas de la sphère unité.

Nous analysons dans ce projet plusieurs relations d'ordre sur la sphère unité, qui conduisent à différentes formulations des opérateurs morphologiques adaptées à la configuration des données. Les notions de supremum et infimum locaux sont introduites, qui permettent de définir les opérateurs de dilatation et d'érosion. Des opérateurs associés à des ordres supervisés sont en particulier considérés pour les questions de reconnaissance de cibles. Nous présentons également différentes procédures de filtrage à des fins de débruitage. Les différentes méthodes étudiées au cours de ce projet s'inscrivent dans le cadre de la généralisation des opérateurs morphologiques à la géométrie intrinsèque de la sphère. L'analyse effectuée conduit à une compréhension extensive des données, qui permet l'automatisation de la détection de cibles.

Mots-clés: Traitement d'image, Morphologie mathématique, Sphère, SAR Processing, Polarimétrie

Resum del projecte

Títol: Morfologia matemàtica a l'esfera: Aplicació a tractament d'Imatges Polarimètriques

Autor: Joana Maria Frontera Pons

Departament: Centre de morphologie mathématique

Director: Dr. Jesús Angulo

Resum:

El radar d'obertura sintètica totalment polarimètric (PolSAR) proporciona dades que contenen la informació completa de dispersió. Aquestes dades han captat més atenció en els últims anys. Les dades PolSAR poden ser representades com a estats de polarització en una esfera. Es presenten tècniques de processament d'imatge basades en l'anàlisi de la informació polarimètrica i en la seva ubicació en l'esfera.

La morfologia matemàtica és una tècnica no lineal per al processament d'imatges. Es basa en el càlcul dels valors mínim i màxim al voltant d'un punt. Precisa de l'existència d'una relació d'ordre entre els punts a tractar. La manca d'un ordre natural en l'esfera presenta un problema inherent a l'hora de definir els operadors morfològics estesos a l'esfera unitat. En aquest projecte s'analitzen algunes propostes per al problema de l'ordre en l'esfera unitat, el que dona lloc a formulacions dels operadors morfològics adaptats a la configuració de les dades. S'introdueix la noció de suprem i ínfim local, el que permet definir la dilatació i l'erosió en l'esfera. Considerem ordres supervisats i els seus operadors associats per a problemes de reconeixement d'objectius. També es presenten diversos procediments de filtratge per a la eliminació de soroll. Els diferents mètodes estudiats en aquest projecte busquen la generalització dels operadors morfològics a l'esfera. Mitjançant l'anàlisi realitzat, es pretén aconseguir la comprensió de les dades i l'automatització en la detecció de blancs.

Paraules clau: Tractament d'imatge, Morfologia matemàtica, Esfera, Processament SAR, Polarimetria

Resumen del proyecto

Títulol: Morfología matemática en la esfera: Aplicación a Procesado de Imágenes Polarimétricas

Autor: Joana Maria Frontera Pons

Departamento: Centre de morphologie mathématique

Director: Dr. Jesús Angulo

Resumen:

El radar de apertura sintética totalmente polarimétrico (PolSAR) proporciona datos que contienen la información completa de dispersión. Estos datos han captado más atención en los últimos años. Los datos PolSAR pueden ser representados como estados de polarización en una esfera. Se presentan las técnicas de procesamiento de imágenes basadas en el análisis de la información polarimétrica y en su ubicación en la esfera.

La morfología matemática es una técnica no lineal para el procesamiento de imágenes. Se basa en el cálculo de los valores mínimo y máximo alrededor de un punto. Precisa de la existencia de una relación de orden entre los puntos a tratar. La falta de un orden natural en la esfera presenta un problema inherente a la hora de definir los operadores morfológicos extendidos a la esfera unidad. En este proyecto se analizan algunas propuestas para el problema del orden en la esfera unidad, lo que da lugar a formulaciones de los operadores morfológicos adaptados a la configuración de los datos. Se introduce la noción de supremo e ínfimo local, lo que permite definir la dilatación y la erosión en la esfera. Consideramos órdenes supervisados y sus operadores asociados para problemas de reconocimiento de objetivos. También se presentan varios procedimientos de filtrado para la eliminación de ruido. Los diferentes métodos estudiados en este proyecto persiguen la generalización de los operadores morfológicos a la esfera. A través del análisis realizado, se pretende lograr una comprensión de los datos y la automatización en la detección de blancos.

Palabras clave: Procesado de Imagen, Morfología matemática, Esfera, Procesado SAR, Polarimetría

Contents

1	Introduction	15
1.1	Objectives of this Master Thesis	15
1.2	Polarimetric Radar Data and its various representations	16
1.2.1	Introduction	16
1.2.2	The Polarization Ellipse	16
1.2.3	Polarization in Radar Systems	17
1.2.4	The Polarization State	18
1.2.5	Polarimetric Scattering	19
1.2.6	Scattering Matrix	19
1.2.7	Polarimetric Data in the Power Domain	20
1.3	The Sphere \mathbb{S}^2	20
1.3.1	Distance on the sphere	21
1.4	Examples of images valued on \mathbb{S}^2	22
1.5	Image and data processing for polarimetric data	23
1.6	Organisation of the document	23
2	Averaging-based filtering on images valued on \mathbb{S}^2	27
2.1	Vector Mean and Median	27
2.2	Fréchet-Karcher Barycenter	30
2.3	Bilateral filtering for \mathbb{S}^2 -valued images	35
2.3.1	Trilateral filtering	37
3	Short review on morphological operators for scalar images	40
3.1	Scalar images	40
3.2	Dilation and erosion	40
3.3	Opening and closing	42
4	Morphological residues-based on distances as target detectors	43
4.1	Nonlinear-gradient based on distances	43
4.2	Top-hat based on distances	46

4.3	Application to target detection	48
5	Supremum and infimum on \mathbb{S}^2	52
5.1	Local origin on the sphere and supremum/infimum computation on tangent space	52
5.1.1	Supremum	53
5.1.2	Infimum	56
5.2	Pseudo-dilation and pseudo-erosion	59
5.2.1	Definition of sup/inf-based operators	59
5.2.2	Some properties and their use	59
5.3	Derived operators	62
5.3.1	Gradient on the sphere	62
5.3.2	Pseudo-opening and pseudo-closing on the sphere	62
5.3.3	Top-hat on the sphere	62
5.3.4	Contrast on the sphere	64
5.4	Conclusions and perspectives	64
6	Supervised ordering on \mathbb{S}^2	68
6.1	Complete lattices in \mathbb{S}^2	68
6.1.1	h-supervised orderings on \mathbb{S}^2	69
6.2	Mathematical morphology in Complete Lattices	72
6.3	Hit-or-miss transform	72
6.3.1	Supervised hit-or-miss transformation in \mathbb{S}^2	73
6.4	Supervised opening and supervised top-hat	76
6.4.1	Restricted supervised top-hat in \mathbb{S}^2	76
6.5	Conclusions and perspectives	77
7	Conclusions and perspectives	79
7.1	Main contributions	79
7.2	Future work	80

Chapter 1

Introduction

1.1 Objectives of this Master Thesis

This report is the result of our master thesis project carried out in the Centre de Morphologie Mathématique at MINES ParisTech, France.

The methodological aim of this project is to explore the generalization of mathematical morphology operators to images valued in the unit sphere of \mathbb{R}^3 .

It is well known in the state-of-the-art of signal and image processing that mathematical morphology is a nonlinear approach based on the computation of minimum and maximum values of local neighborhoods. That requires the existence of an ordering between the points to select the maximum or the minimum between them. It is also obvious that there is no natural ordering in the sphere and consequently there is no straightforward generalization of morphological operators to the sphere.

In this context, we have introduced in the project some original contributions to the problem of ordering on the unit sphere which allow us defining morphological (or pseudo-morphological) filters for images valued on the sphere. Some of our ideas are inspired from the works on morphology on the unit circle [11], but most of results introduce a new insight into ordering for this kind of non Euclidean valued space.

The values on the unit sphere may represent different kinds of physical information. In imaging applications, the most classical case is the orientation images, obtained after estimating the local orientation of each pixel. In modern medical imaging, High Angular Resolution Imaging (HARDI) produces also images with values on the sphere. Nevertheless the application domain considered in the project is the polarimetric radar data defined on spatial support (a 2D space).

Hence, the next paragraph of this introduction chapter is devoted to a remind about polarimetric radar data and its various representations, which allow us to interpret the sphere-valued images as polarimetric images (polarization states on Poincaré sphere). We have used mainly simulated images for the pedagogical examples which illustrate the developments of

the project. Consequently, a validation of the methods on real polarimetric radar images is required. In spite of this lack of validation, we consider that the application of morphological operators may yield to innovative algorithms in different radar applications: denoising and target detection in uneven backgrounds, segmentation of radar clutters, etc.

1.2 Polarimetric Radar Data and its various representations

1.2.1 Introduction

In an electromagnetic plane wave, Electric and Magnetic fields have a temporal variation in the plane perpendicular to the direction of travel. The two fields are orthogonal to one another, and are described by Maxwell's equations. We need three parameters to describe the propagation of EM waves in a medium: dielectric constant, permeability and conductivity. In general, far enough from the source of the wave, we assume the wavefront is flat, as it is contained on a plane. Polarization refers to the alignment and regularity of the Electric and Magnetic fields in the plane perpendicular to the propagation direction.

The electromagnetic wave is characterized by the behavior of the Electric field vector as a time depending function. The waveform can be deterministic or random, or a combination of both of them. Random wave is like pure noise, and deterministic wave can be formulated as a sine wave. An electromagnetic wave, without random component is called completely polarized.

1.2.2 The Polarization Ellipse

The Electric field of a plane wave is described as the sum of two orthogonal components (horizontal and vertical). Each one with different amplitude and phase, being able to define a relative phase between them. The tip of Electric field vector of a totally polarized wave describes a regular pattern, in general cases elliptical.

The angle between the semi-major axis and the positive x-axis measured counter-clockwise is the "orientation", ψ . It can take values between 0° and 180° . The shape parameter to describe the oval is called eccentricity or "ellipticity", defined as

$$\chi = \arctan(b/a) \quad (1.1)$$

And it lies within $[-45^\circ, 45^\circ]$. The shape of the ellipse is linked to the amplitude and relative phase between horizontal and vertical components.

- When components are in phase, the polarization is linear, $\chi = 0$

$$\Delta\phi = 2k\pi$$

As components may have different amplitudes, orientation can take any value. The two linear polarizations in common use are:

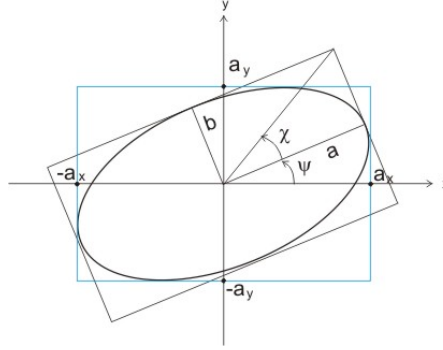


Figure 1.1: Polarization ellipse.

- $\psi=0^\circ, 180^\circ$ Horizontal linear polarization ($E_y=0$)
- $\psi=90^\circ$ Vertical linear polarization ($E_x=0$)
- When relative phase is 90° , and horizontal and vertical components are equal, polarization is circular.

$$\Delta\phi = (2k + 1)\frac{\pi}{2}$$

$$E_x = E_y$$

Orientation is not defined. Then if

- $\psi=45^\circ$ Left circular polarization
- $\psi=-45^\circ$ Right circular polarization

Observing the wave along the direction of propagation, the polarization is left-handed if the rotation of the Electric Field vector is counter-clockwise.

In SAR system analysis, we usually assume there is a single carrier. This is a valid approach, as SAR systems usually have very narrow bandwidth.

1.2.3 Polarization in Radar Systems

In a radar, the antenna transmits and receives EM waves of a specific polarization. The transmitted wave is almost purely polarized (with a certain known polarization). In some simple radar systems, the same antenna is configured to receive the polarization it has been sent.

A basis polarizations are needed to create any polarization. The two most common polarizations are horizontal linear(H), and vertical linear(V). Circular polarizations Right(R) and Left(L) Hand can also be used as basis. In more complex systems, the antenna can

transmit and receive more than one polarization. In transmission can be combined H and V components, creating, for example, a circular polarization. The scattered wave may present different polarization from the incident wave. The radar antenna is often designed to receive the different polarization components of the wave. For example, the H and V parts of the antenna can receive the two orthogonal components of the incoming wave and process them separately.

In a radar system using H and V linear polarizations, we have the following channels:

- **HH** for horizontal transmit and horizontal received (*like-polarized*)
- **VV** for vertical transmit and vertical received (*like-polarized*)
- **HV** for horizontal transmit and vertical received (*cross-polarized*)
- **VH** for vertical transmit and horizontal received (*cross-polarized*)

A radar system has different levels of complexity of polarizations:

- Single polarized - HH or VV or HV or VH
- Dual polarized - HH and HV, VV and VH, or HH and VV
- Four polarizations - HH, VV, HV and VH

A polarimetric radar uses the four polarizations channels and measures the phase difference and the amplitude. Some dual polarized radars also measure the phase difference between channels, this parameter plays a key role in polarimetric information extraction.

1.2.4 The Polarization State

The polarization state of a plane wave is described by orientation, ψ and ellipticity χ and a parameter S_0 proportional to the total intensity of the wave. Gabriel Stokes described the polarization state of the EM wave by a vector, known as the Stokes vector:

$$\begin{bmatrix} S_0 \\ S_1 \\ S_2 \\ S_3 \end{bmatrix} = \begin{bmatrix} |E_v|^2 + |E_h|^2 \\ |E_v|^2 - |E_h|^2 \\ 2\Re\{E_v E_h^*\} \\ 2\Im\{E_v E_h^*\} \end{bmatrix} = \begin{bmatrix} S_0 \\ S_0 \cos 2\psi \cos 2\chi \\ S_0 \sin 2\psi \cos 2\chi \\ S_0 \sin 2\chi \end{bmatrix} \quad (1.2)$$

An EM plane wave can be completely polarized, partially polarized or completely unpolarized. If it is totally polarized, only three of the Stokes parameters are independent, because of the total power relation,

$$S_0^2 = S_1^2 + S_2^2 + S_3^2 \quad (1.3)$$

If the wave is partially polarized we can rewrite it as the sum of a completely polarized wave and a completely unpolarized (noise). The degree of polarization is the relation between the power of the polarized wave and the total power. Written according to the Stokes parameters

$$\frac{\sqrt{S_1^2 + S_2^2 + S_3^2}}{S_0} \quad (1.4)$$

1.2.5 Polarimetric Scattering

We introduce how an EM wave having a certain polarization is scattered by a target. The scattering properties of a target are measured with a polarimetric radar. The radar illuminates the target with an incident wave that is scattered by the target. Some of this scattered wave returns to the receiving antenna. The transmitting and receiving antenna are often in the same place, mono-static case, and the energy received is called backscatter. The polarization of the incident wave is known and all polarization properties are measured from the backscattered wave.

A polarimetric radar transmits in two orthogonal polarizations, usually H and V, and receives the backscattered wave in the same two polarizations. It measures the difference in phase and amplitude in the four channels received, where there is all the information to measure the polarimetric scattering properties of the target.

1.2.6 Scattering Matrix

If the incident wave is horizontally polarized, the backscattered wave will have contributions in the vertical and horizontal polarizations. As the components H and V form a basis that can describe the electromagnetic wave, the backscattering properties of the target can be completely described by the scattering matrix, S

$$\begin{bmatrix} E_h^s \\ E_v^s \end{bmatrix} = \begin{bmatrix} S_{hh} & S_{hv} \\ S_{vh} & S_{vv} \end{bmatrix} \begin{bmatrix} E_h^i \\ E_v^i \end{bmatrix} \quad (1.5)$$

The matrix describes the transformation of the electric field. The four elements are complex numbers and are obtained by measuring amplitudes and phases in the four channels of polarimetric radar. A calibration process is needed. Properties described are valid only at that frequency and the beam angle the radar has used. We have to ensure that it is sufficiently representative for the desired scenario. In mono-static radars, the majority of targets have reciprocity, ie. $S_{hv}=S_{vh}$, the scattering matrix is symmetric. As its components are complex, if there is a phase change during the process of dispersion, is represented in the matrix.

1.2.7 Polarimetric Data in the Power Domain

Scattering properties can be represented also in the power domain. These versions of the scattering matrix completely describe the dispersive behavior of the target. The covariance and coherency matrices are the two most widely used representations. Another examples are the Stokes and Mueller Matrices, which also transform the incident wave into the backscattered wave.

The average of adjacent samples is very useful in polarimetric radar, and the analysis of their data. The effect of noise and spots are reduced at the expense of degrading the image resolution. When averaged values in the proximity of a sample, the scatterers that were represented by different samples are consolidated in the image. The spots and noise reduction, and the grouping of scatters facilitate the interpretation of the image. The average is in the domain of power, because it preserves the energy of the individual components in the representations of power (this does not happen in voltage). In general, the average is a post-processing operation, values of the power matrix adjacent samples are averaged. You can reduce the volume of data and can be used to create equally spaced pixels in ground range and azimuth. It also supports the representation of several dispersive mechanisms and noise.

1.3 The Sphere \mathbb{S}^2

For a completely polarized wave, the polarization state can be described by a point on the Poincaré sphere. The radius of the sphere is S_0 , the intensity of the wave. The latitude of the point corresponds to 2χ and the longitude to 2ψ , see Fig.1.3(a). Then the linear polarizations lie on the equator, with horizontal and vertical polarizations opposite each other. Moreover, left-hand circular and right-hand circular polarizations are placed on the north and south poles respectively, see Fig.1.3(b). All other points represent elliptical polarization with certain χ and ψ . Opposite points on the sphere, antipodal points, represent polarizations that are orthogonal to one another and are called cross-polarizations. To place the polarization on the sphere, we represent the last three Stokes parameters as components in a three-dimensional vector space, as in Fig.1.3(a).

The four dimensional Stokes vector can be also interpreted as four-vectors of Minkowski space. Then all possible polarization states correspond to time-like, future-directed vectors.

As mentioned above, the sphere \mathbb{S}^2 is also the space of definition for 3D orientation information and consequently, all the methods discussed in the project are not limited to the polarimetry and can be applied, without any modification, to orientation-valued images, e.g., 3D images of vector gradient, HARDI images, etc.

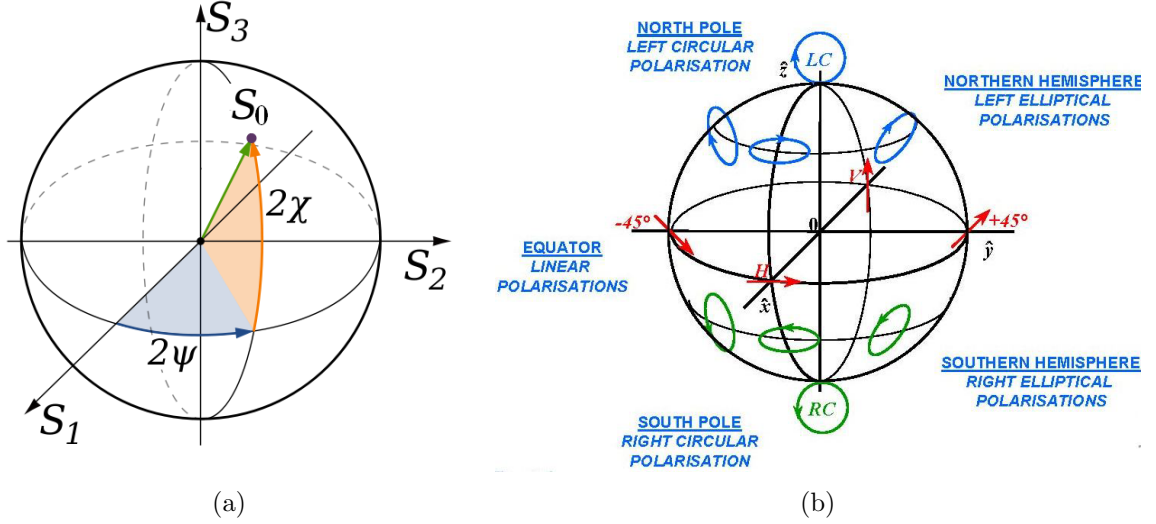


Figure 1.2: (a) Stokes parameters and latitude/longitude on the sphere. (b) Polarization states on the Poincaré sphere.

1.3.1 Distance on the sphere

Let $\xi_i, \xi_j \in \mathbb{S}^2$ be two points lying on the sphere, which are not antipodal points. The shortest distance between them is the one measured along a path on the surface of the sphere; rather than going through the interior of the sphere. In non-Euclidean geometry, straight lines have to be replaced with their correspondent geodesics.

On the sphere the geodesics are the great circles, circles whose center is the same as that of the sphere. The two points separate the great circle into two arcs. The length of the shortest arc is the distance to determine. For a sphere of radius one, we can formulate,

$$d(\xi_i, \xi_j) = \arccos(\xi_i \cdot \xi_j) \quad (1.6)$$

$$d(\xi_i, \xi_j) = \arcsin(|\xi_i \times \xi_j|) \quad (1.7)$$

$$d(\xi_i, \xi_j) = \arctan\left(\frac{|\xi_i \times \xi_j|}{\xi_i \cdot \xi_j}\right) \quad (1.8)$$

where \cdot denotes the scalar (or dot) product and \times the vector (or cross) product. The expression (1.8) using computation function `atan2` gives more accurate results and is the one used when a distance on the sphere is referred. If the radius of the sphere is not one, simply multiply the distance obtained by the value of the radius.

1.4 Examples of images valued on \mathbb{S}^2

The proposed methods and morphological operators in this project are related to data lying on the surface of a sphere. The examples analyzed are simulated images presenting a simple scenario, with several targets of different sizes to be detected.

An image valued on the sphere is a mapping from the space of pixels E , the *support space* of the image, onto the sphere:

$$f(x, y) = \begin{cases} E & \longrightarrow \mathbb{S}^2 \\ (x, y) & \longmapsto \xi_i \end{cases}$$

Let us denote by $\mathcal{F}(E, \mathbb{S}^2)$ the space of 2D images with pixel values on the sphere: $f(x, y) \in \mathcal{F}(E, \mathbb{S}^2)$. Typically, for 2D image the support space of pixels is $E \subset \mathbb{Z}^2$. The data placed in a position of the sphere represent a specific polarization state. These values onto the sphere \mathbb{S}^2 are given in their 3D coordinates:

$$\xi_i = (s_{1,i}, s_{2,i}, s_{3,i}) : \sqrt{s_{1,i}^2 + s_{2,i}^2 + s_{3,i}^2} = 1$$

Therefore the images valued on the sphere can be considered as a 3-component image, i.e.,

$$f(x, y) = (f_{S_1}(x, y), f_{S_2}(x, y), f_{S_3}(x, y))$$

where each component represents the values for each coordinate of the 3D space, i.e., $f(x, y) = \xi_i \Leftrightarrow f_{S_j}(x, y) = s_{j,i}$, for $j = 1, 2, 3$.

The developed operators, for instance ϑ , involve a processing of images according to this representation, i.e.,

$$\vartheta : \begin{cases} \mathcal{F}(E, \mathbb{S}^2) \rightarrow \mathcal{F}(E, \mathbb{S}^2) \\ g(x, y) = \vartheta(f)(x, y) \end{cases}$$

where $f(x, y)$ is the input image and $g(x, y)$ is the output image, result of processing $f(x, y)$ with operator ϑ .

Fig. 1.3 provides a typical example of polarimetric simulated image which has been used in this project, which includes objects (target) of different sizes, with different values onto the sphere and an homogeneous background (clutter). Then, various levels of “noise” are also considered in the simulated examples, also with different dispersions, and example can be observed in Fig. 1.4

Another example used in the illustration, which has more complexity is the one given in Fig. 1.5. In this case, there are three different clutters represented and three types of targets, with their corresponding states of polarization.

We point out that in order to illustrate the results obtained by the different filters and transformations, 2D images corresponding exclusively to one of the components are displayed in the examples.

1.5 Image and data processing for polarimetric data

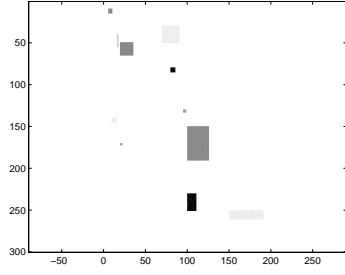
Polarimetric radar processing is already well established methodology, see for instance the excellent monograph [16].

Concerning the application of image processing tools for the analysis of polarimetric data, the state-of-the-art is still limited, can correspond mainly to the used of pixel-based classification techniques. For instance, [29], [32].

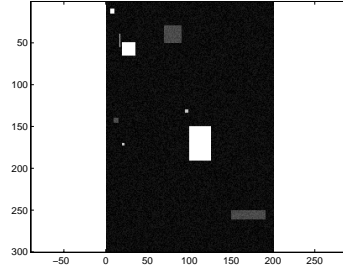
1.6 Organisation of the document

The report of this Master thesis is organized into the following chapters.

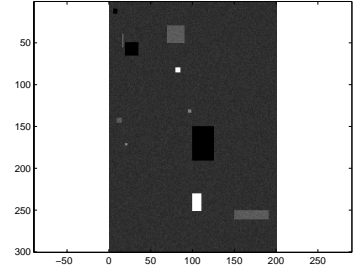
- In chapter 2, various methods are proposed for filtering images valued on \mathbb{S}^2 and some examples that show the performance of different filters.
- A background on the basic morphological operators for scalar images is given in chapter 3. This short review is necessary to fix the notation and to make easier the definition of the new operators for images valued on \mathbb{S}^2 .
- Chapter 4 discusses the use of morphological operators such as gradient and the top-hat and its application to detection of targets in \mathbb{S}^2 -valued radar data.
- Chapter 5 poses the need for a partial ordering on \mathbb{S}^2 and proposes a solution based on the notion of local supremum/infimum, which allows to introduce the (pseudo-) dilation/erosion on the sphere. The interest for image enhancement and target detection is considered.
- Chapter 6 deals with supervised ordering on \mathbb{S}^2 , which yields a rich framework for the generalization of all morphological operators on the sphere. In particular, supervised openings/closings and supervised hit-or-miss are introduced. Various strategies on the computation of the supervised ordering are considered and the different alternatives are studied for the purpose of target detection.



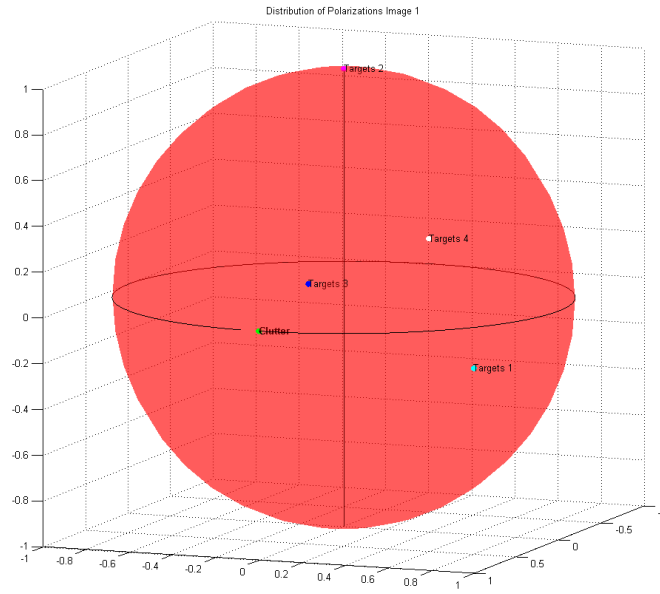
(a) $f_{S_1}(x, y)$



(b) $f_{S_2}(x, y)$



(c) $f_{S_3}(x, y)$



(d)

Figure 1.3: Simulated image, valued on the sphere $f(x, y) \in \mathcal{F}(E, \mathbb{S}^2)$ and used to illustrate the proposed methods: (a) (b) and (c) show the value of each of the coordinates in \mathbb{R}^2 . While their situation on \mathbb{S}^2 and the corresponding polarization states are displayed in (d).

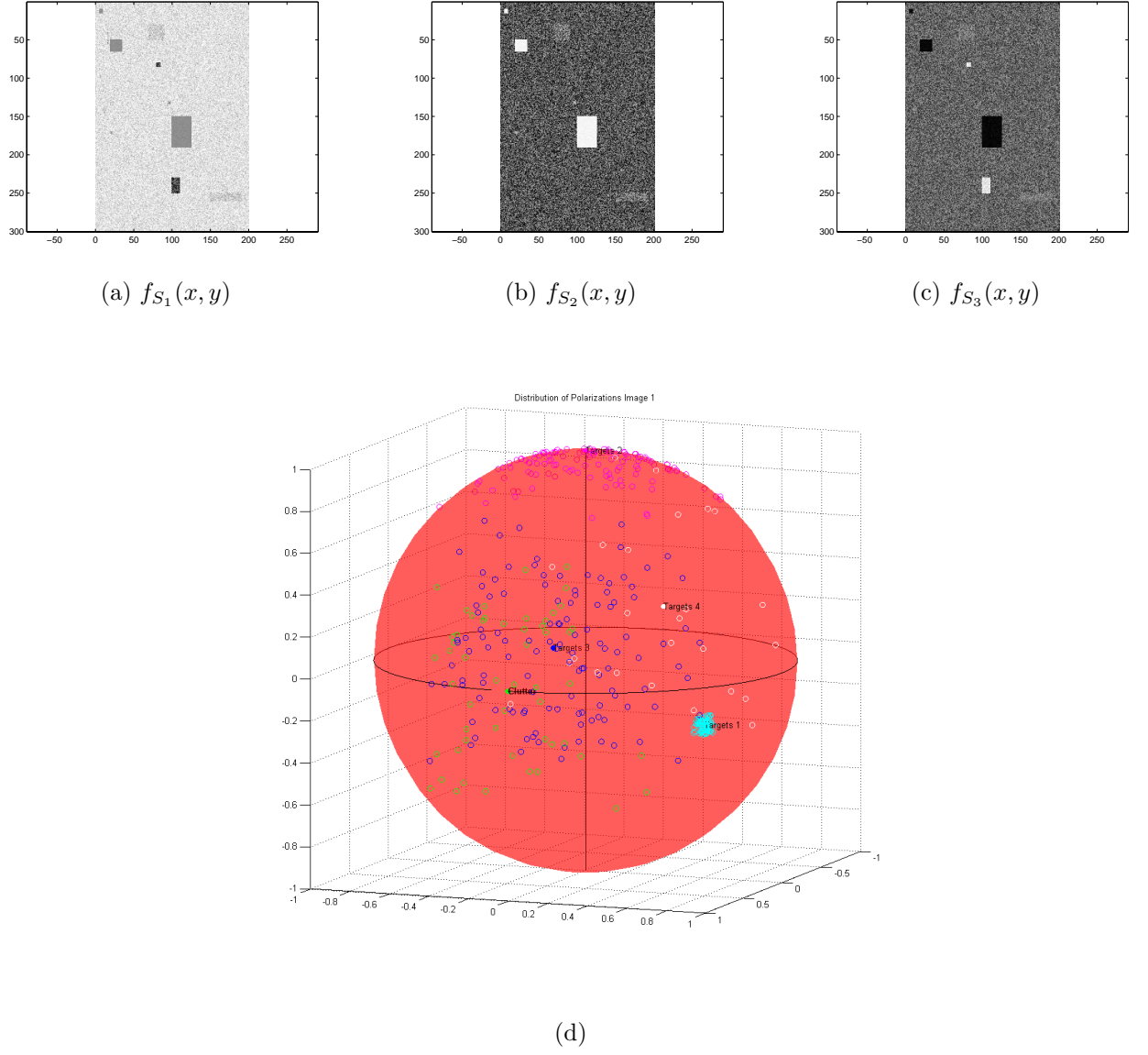
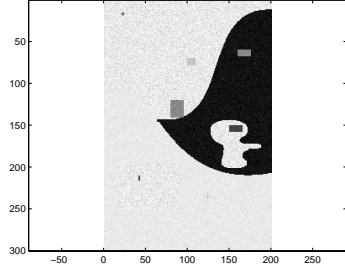
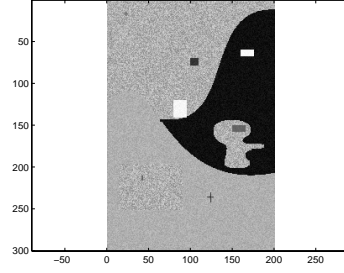


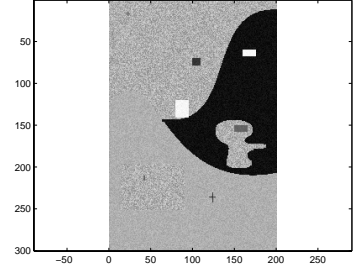
Figure 1.4: Image valued on \mathbb{S}^2 with a higher degree of noise.



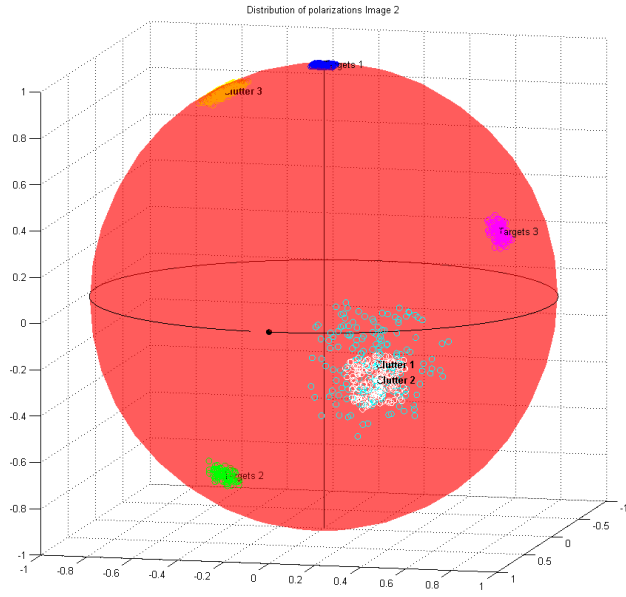
(a) $f_{S_1}(x, y)$



(b) $f_{S_2}(x, y)$



(c) $f_{S_3}(x, y)$



(d)

Figure 1.5: Image valued on \mathbb{S}^2 that shows a more complex scenario with several types of targets and clutters.

Chapter 2

Averaging-based filtering on images valued on \mathbb{S}^2

By the nature of polarimetric radar, the corresponding data to be processed are very noisy. It is necessary therefore a pre-filtering stage in order to denoise as well as possible, but preserving also the structures of the image (targets, changes in clutter, etc.). We propose the following methods appropriate to the nature of radar data defined on \mathbb{S}^2 .

2.1 Vector Mean and Median

Let us consider that we have set R of N points from \mathbb{S}^2 : $R = \{\xi_i\}_{i=1}^N$, with $\xi_i = (s_{1,i}, s_{2,i}, s_{3,i})$. The simplest form of averaging is to compute the arithmetic mean of each component, i.e.,

$$\mu(R) = \left(\frac{1}{N} \sum_1^N s_{1,i}, \frac{1}{N} \sum_1^N s_{2,i}, \frac{1}{N} \sum_1^N s_{3,i} \right)$$

If this value exists, arithmetic averaging estimates the true expected value in an unbiased manner. The vector obtained minimizes the sum of squared Euclidean distances between the mean and the sample data set since the following expression is valid for each vectorial component:

$$\mu(x_1, \dots, x_N) \stackrel{def}{=} \arg \min_{x \in \mathbb{R}} \frac{1}{N} \sum_{i=1}^N (x - x_i)^2$$

It may happen that the mean value $\mu(R)$ does not correspond to any of the original elements of the set. Moreover, as we average points lying on the sphere, the result is possible to drop into the sphere.

In order to the average vector remains on the surface of the sphere, the median can be considered as an alternative. Median is defined as the value separating higher half of the

sample set, from the lower part; which can also be obtained as a central point that minimizes the average of the absolute deviations:

$$\text{med}(x_1, \dots, x_N) \stackrel{\text{def}}{=} \arg \min_{x \in \mathbb{R}} \frac{1}{N} \sum_{i=1}^N |x - x_i|$$

This definition has been adapted to vector spaces and the vector median [1] of a set of points is defined as the one that minimizes the accumulated distances between vectors. It can be also considered for our problem on \mathbb{S}^2 as follows:

$$\text{med}(R) = \arg \min_{\xi_k \in R} \sum_{i=1}^N d(\xi_i, \xi_k)$$

We notice that according to this definition, the value of the median is one of the elements of the initial set, i.e., $\text{med}(R) \in R$. Therefore, if the distribution of the set has a large dispersion, median is often unrepresentative. Furthermore, vector median has a large computational cost: we should compute all the pairs of distances between the point of R .

Fig. 2.1 provided two examples of point distributions on \mathbb{S}^2 and the corresponding vector mean and median obtained for each set of points.

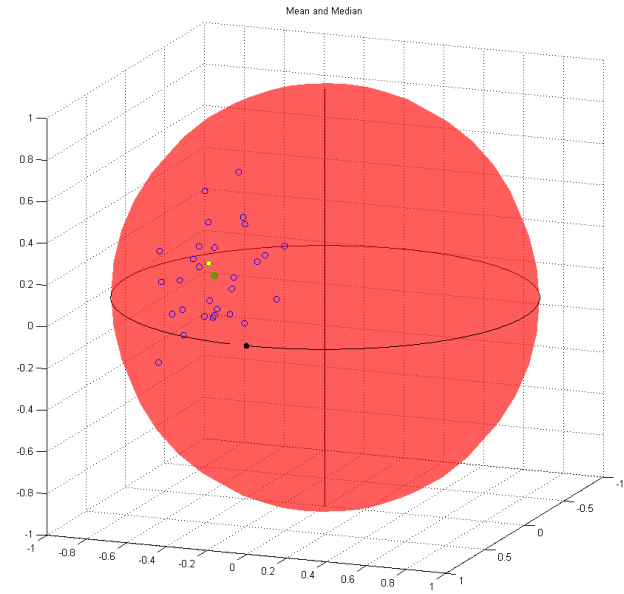
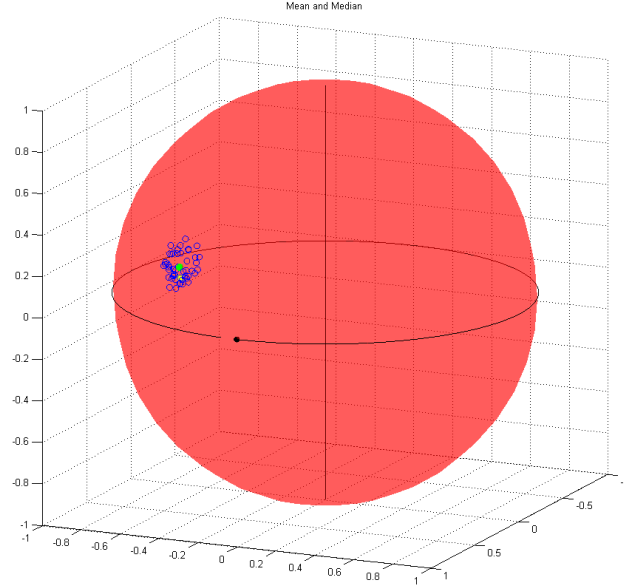


Figure 2.1: The two sets show different distributions on \mathbb{S}^2 . In yellow, the median value and in green, the mean, which is located inside the sphere.

2.2 Fréchet-Karcher Barycenter

A more suitable approach for averaging over the unit sphere is given by using the Fréchet mean. Fréchet mean minimizes the sum of squared distances along geodesics on Riemannian manifolds [9] [13], i.e., for a given set of points $R = \{\xi_i\}_{i=1}^N$ on the sphere, we have

$$\mu^\circ(R) = \arg \min_{\xi \in \mathbb{S}^2} \sum_{i=1}^N d(\xi_i, \xi)^2 \quad (2.1)$$

The problem of computation of the Fréchet mean on the sphere μ° have studied in various works [4] [18] [2] [8] including the recent paper [7], and it is usually solved using a gradient descent method as proposed by Karcher [13]. Some of the properties of unicity were particularly studied in [4]

At every point $\xi_i \in \mathbb{S}^2$, with the Riemannian metric induced by the Euclidean metric on \mathbb{R}^3 , the linear space $T_{\xi_i}\mathbb{S}^2$ tangent to the sphere is given by the exponential map $\exp_{\xi_i}(\vec{\nu}_j)$ at ξ_i , such that $T_{\xi_i}\mathbb{S}^2 = \left\{ \vec{\nu}_j \in \mathbb{R}^3 : \vec{\nu}_j^T \cdot \xi_i = 0 \right\}$, where the vector point is $\vec{\nu}_j = (\nu_{1,j}, \nu_{2,j}, \nu_{3,j})$. We note also that the exponential map \exp_ξ is defined by the correspondence $\vec{\nu} \mapsto \gamma_{\vec{\nu}}(1)$, where $\gamma_{\vec{\nu}} : t \mapsto \gamma_{\vec{\nu}}(t)$ is the unique geodesic satisfying for initial point $\gamma_{\vec{\nu}}(0) = \xi$ and initial tangent vector $\dot{\gamma}(0) = \vec{\nu}$, provided $\gamma_{\vec{\nu}}(t)$ extends at least to $t = 1$.

The method to estimate the Fréchet mean on a sphere consists first projecting the points $\xi_i \in \mathbb{S}^2$ onto a tangent plane $T_{\mathbf{y}_t}\mathbb{S}^2$ at an initial point $\mathbf{y}_t \in \mathbb{S}^2$ by an inverse projection

$$\vec{\nu}_i = \exp_{\mathbf{y}_t}^{-1}(\xi_i) \quad (2.2)$$

where $\vec{\nu}_i \in \mathbb{R}^3$. Then, an expectation $\mathbb{E}[\cdot]$ is calculated on the tangent plane $T_{\mathbf{y}_t}\mathbb{S}^2$ and projected back onto \mathbb{S}^2 by a projection $\exp_{\mathbf{y}_t}$, i.e.,

$$\mathbf{y}_{t+1} = \exp_{\mathbf{y}_t} \left(\mathbb{E} \left[\{\tilde{\nu}_i\}_{i=1}^N \right] \right) \quad (2.3)$$

where

$$\mathbb{E} \left[\{\tilde{\nu}_i\}_{i=1}^N \right] = \left(\frac{1}{N} \sum_1^N \nu_{1,i}, \frac{1}{N} \sum_1^N \nu_{2,i}, \frac{1}{N} \sum_1^N \nu_{3,i} \right)$$

For the unit sphere \mathbb{S}^2 , with the Riemannian metric induced by the Euclidian metric on \mathbb{R}^3 , the inverse exponential map (or logarithmic map) is given by

$$\exp_{\mathbf{y}}^{-1}(\xi) = [1 - (\mathbf{y} \cdot \xi)^2]^{-1/2} (\xi - (\mathbf{y} \cdot \xi)\mathbf{y}) \arccos(\mathbf{y} \cdot \xi) \quad (2.4)$$

where $\mathbf{y}, \xi \in \mathbb{S}^2$. The explicit expression for the exponential map is

$$\exp_{\mathbf{y}}(\vec{\nu}) = \cos(\|\vec{\nu}\|)\mathbf{y} + \sin(\|\vec{\nu}\|) \frac{\vec{\nu}}{\|\vec{\nu}\|} \quad (2.5)$$

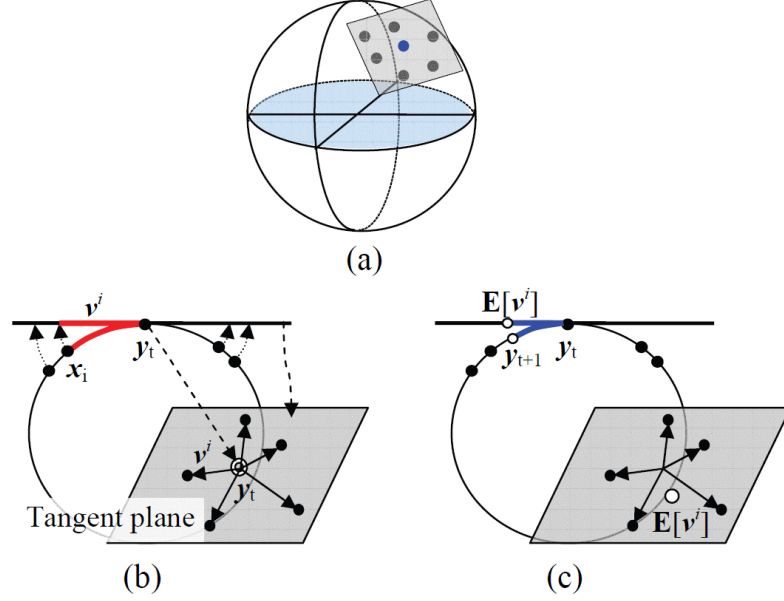


Figure 2.2: Iterative method for computing the Fréchet mean for data on the sphere: (a) All the points are projected onto the plane tangent (b) at the starting point y_t (c) an expectation is calculated on the tangent space and the result is projected back onto the sphere.

where $\vec{v} \in T_y \mathbb{S}^2$ and $\vec{v} \neq (0, 0, 0)$

Using t as an iteration index, Eq. (2.2) and (2.3) leads to a gradient descent iterative algorithm. Choosing an appropriate starting point y_0 the algorithm converges within a few iterations to the Fréchet mean:

$$y_T = \mu^\circ(R)$$

such that $y_{T+1} = y_T$. When the set has a low dispersion and data are concentrated around a “barycenter”, Fréchet mean converges within one or two iterations. In these cases the value is nearly the same as the mean and median. Figure 2.3 shows an example where the data are widely scattered over the sphere, and the evolution up to the mean value μ° .

The Fréchet mean can be now used to define an averaging filter for images valued on the sphere. Hence, given an image $f \in \mathcal{F}(E, \mathbb{S}^2)$, we define the *Fréchet mean filter on the sphere* as the following operator

$$M_B^\circ(f)(x, y) = \{\mu^\circ([f(v, w)]); (v, w) \in B(x, y)\}$$

where B is the window which defines the averaging zone for each pixel and $B(x, y)$ is the neighbourhood centered at pixel (x, y) .

Fig. 2.4 depicts two examples of noisy images and the corresponding denoising obtained by means of the Fréchet mean filter on the sphere. The improvement is more remarkable if the images are very noisy. Otherwise contours of the objects become fuzzy. Comparing the results with the median filter, the Fréchet mean filtered data are less homogeneous but more robust to aberrant samples, as Fréchet mean gives a good estimate of the barycenter of the set of values belonging to each neighbourhood.

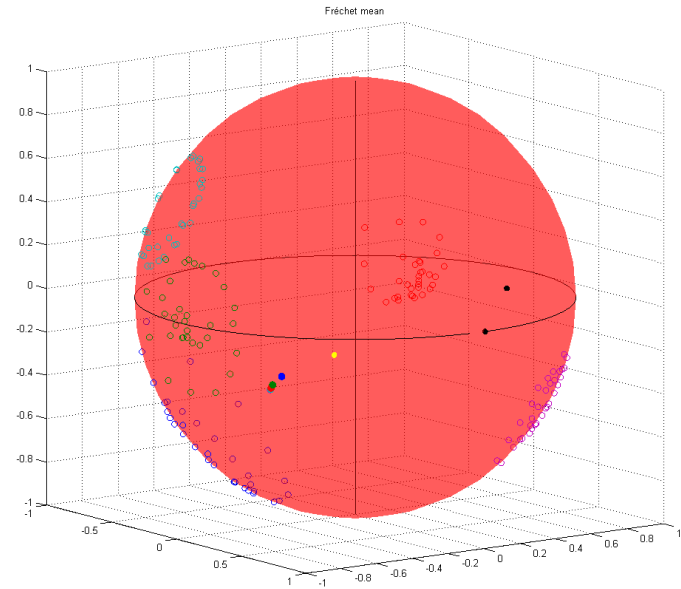
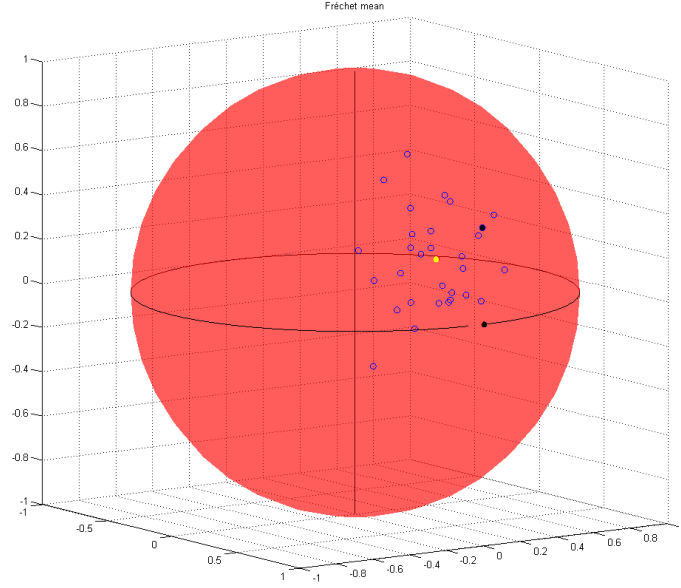
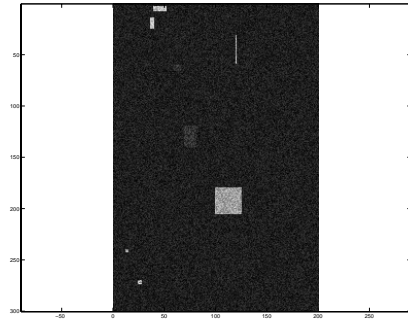
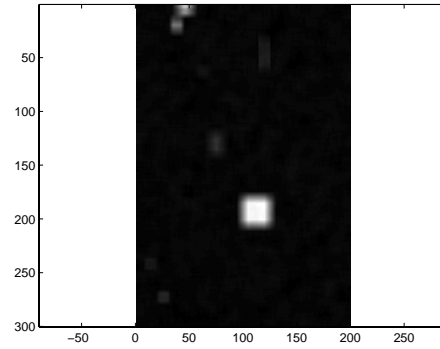


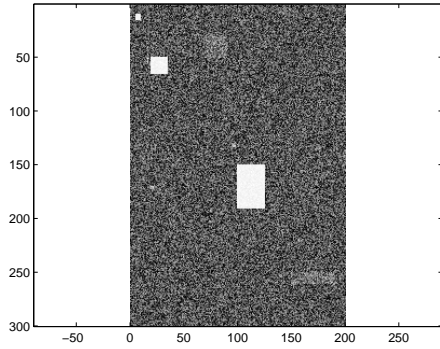
Figure 2.3: Fréchet mean for two sets with different distributions of point on \mathbb{S}^2 . In black the starting point, different colors points correspond to the consecutive iterations until the algorithm converges to the yellow point.



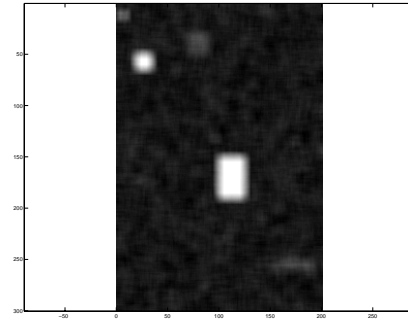
(a) $f_1(x, y)$



(b) $M_B^o(f_1)(x, y)$



(c) $f_2(x, y)$



(d) $M_B^o(f_2)(x, y)$

Figure 2.4: Noisy images and the output of filtering using the Fréchet mean: (a) and (c) original images, (b) and (d) filtered images. The window B is a square of size 5×5 pixels.

2.3 Bilateral filtering for \mathbb{S}^2 -valued images

In the proposed filter $M_B^\circ(f)(x, y)$, each output pixel value is processed jointly with its neighbours, assigning to each one the same fixed weight. An interesting case in image filtering gives more importance to those pixels closer to pixel the window is centered on. The weights are not fixed anymore but they decrease as far as they are to the pixel to treat. These weights are usually computed with a Gaussian kernel $k_\sigma(\tau)$ (other kernels could be used instead) of width parameter σ , i.e.,

$$k_\sigma(\tau) = e^{\frac{-\tau^2}{2\sigma^2}} \quad (2.6)$$

In a particular neighbourhood B centered at pixel (x, y) , the weight for each pixel $(u, v) \in B(x, y)$ is given by $k_\sigma(\tau)$ where $\tau = \sqrt{(x-u)^2 + (y-v)^2}$. Therefore, we define the *Fréchet Gaussian filter on the sphere* as the following operator

$$M_{B,\sigma}^\circ(f)(x, y) = \{\mu_\sigma^\circ([f(v, w)]) ; (v, w) \in B(x, y)\}$$

where μ_σ° is the weighted Fréchet mean using the Gaussian weights, i.e.,

$$\mu_\sigma^\circ([f(v, w)]) = \arg \min_{\xi \in \mathbb{S}^2} \sum_{(u,v) \in B(x,y)} W_\sigma(u, v) d(\xi, f(u, v))^2 \quad (2.7)$$

where

$$W_\sigma(u, v) = \frac{e^{-\frac{(x-u)^2 + (y-v)^2}{2\sigma^2}}}{\sum_{(u,v) \in B(x,y)} e^{-\frac{(x-u)^2 + (y-v)^2}{2\sigma^2}}} \quad (2.8)$$

The weighted Fréchet mean defined in Eq. (2.9) can be solved using the iterative gradient descent algorithm, where the effect of the coefficients is introduced once all the neighbours are already projected into the tangent plane, to calculate a weighted average. An example of spatial weighting filtering is given in Fig. 2.5.

A more selective smoothing is obtained if another contribution is introduced in the weight for each neighbour, which depends on the difference between the intensity value of the central pixel and the value of the corresponding neighbour. That corresponds to the definition of the bilateral filter. Bilateral filtering [26] is a locally adaptive Gaussian convolution technique to smooth images while preserving edges, where the Gaussian coefficients at a point are weighted jointly by the spatial distance and the intensity distance between its neighbours. Its formulation is quite simple and requires only two easily tunable parameters: the size and the contrast of the image features to preserve. A recent systematic study on the theory and applications of bilateral filtering can be found in [17]. As it was shown in [6], bilateral filtering is strongly related to weighted least squares filtering [15], robust estimation filtering [31, 3] and anisotropic diffusion [30, 24]. In particular, bilateral filtering is a discrete filter equivalent asymptotically to the Perona and Malik PDE equation [19, 5].

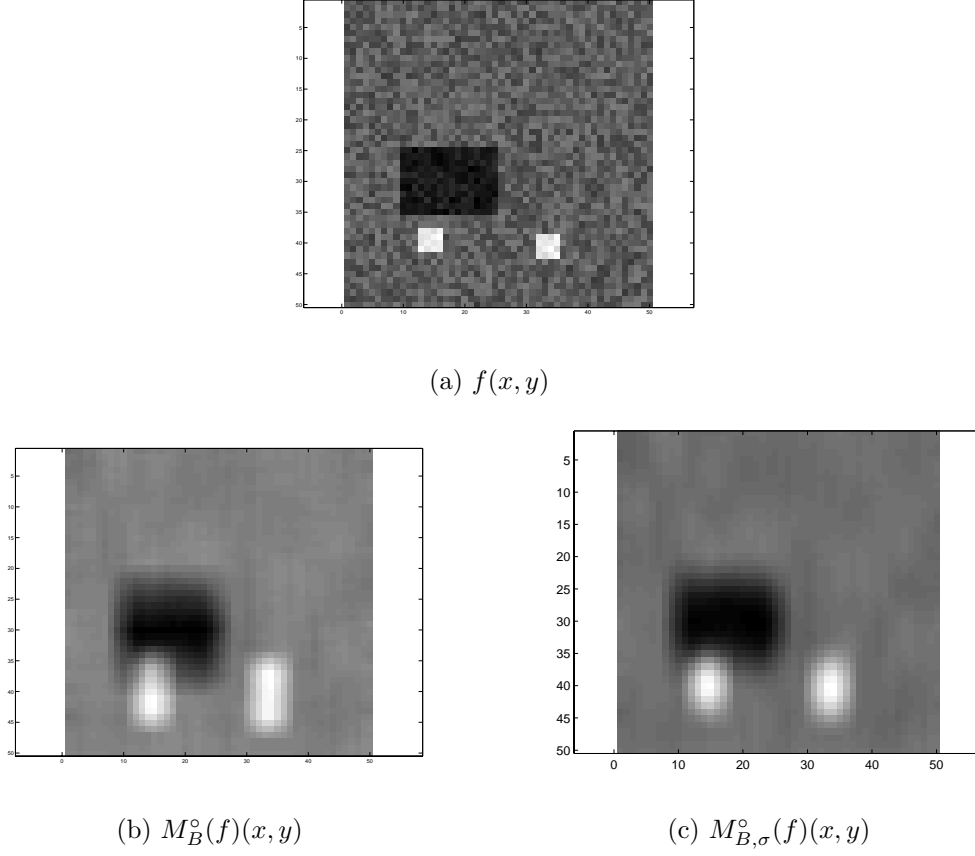


Figure 2.5: Original image (a) and comparison between mean filtering by regular Fréchet mean (b) and by Weighted Fréchet mean with weights in the pixels space E (c). In both cases B is a square of size 5×5 pixels and $\sigma = 0.9$.

The *Fréchet bilateral filter on the sphere* of image $f(x, y) \in \mathcal{F}(E, \mathbb{S}^2)$ is a spatially-variant averaging filter defined as follows:

$$BL_{B, \sigma_s, \sigma_i}^\circ(f)(x, y) = \left\{ \mu_{\sigma_s, \sigma_i}^\circ([f(v, w)]); (v, w) \in B(x, y) \right\}$$

where $\mu_{\sigma_s, \sigma_i}^\circ$ is the weighted Fréchet mean using the bilateral weights, i.e.,

$$\mu_{\sigma_s, \sigma_i}^\circ([f(v, w)]) = \arg \min_{\xi \in \mathbb{S}^2} \sum_{(u, v) \in B(x, y)} W_{\sigma_s, \sigma_i}(u, v) d(\xi, f(u, v))^2 \quad (2.9)$$

where

$$W_{\sigma_s, \sigma_i}(u, v) = \frac{1}{\widetilde{W}(x, y)} e^{-\frac{(x-u)^2 + (y-v)^2}{2\sigma_s^2}} e^{-\frac{d(f(u, v), f(x, y))^2}{2\sigma_i^2}} \quad (2.10)$$

and $\widetilde{W}(x, y)$ is the normalization factor

$$\widetilde{W}(x, y) = \sum_{(u, v) \in B(x, y)} W_{\sigma_s, \sigma_i}(u, v)$$

The pair of width parameters defines the vector scale (σ_s, σ_i) , with σ_s is the spatial (or size) scale and σ_i the intensity (or tonal or range) scale. The intensity distances are computed as the distance between two points on the sphere. It is also possible to measure the difference on the tangent plane. Thus the distance becomes a regular Euclidean distance. By adding the intensity component and combining it with the distance dependent component, the points far on the sphere from the pixel of interest will have a small contribution.

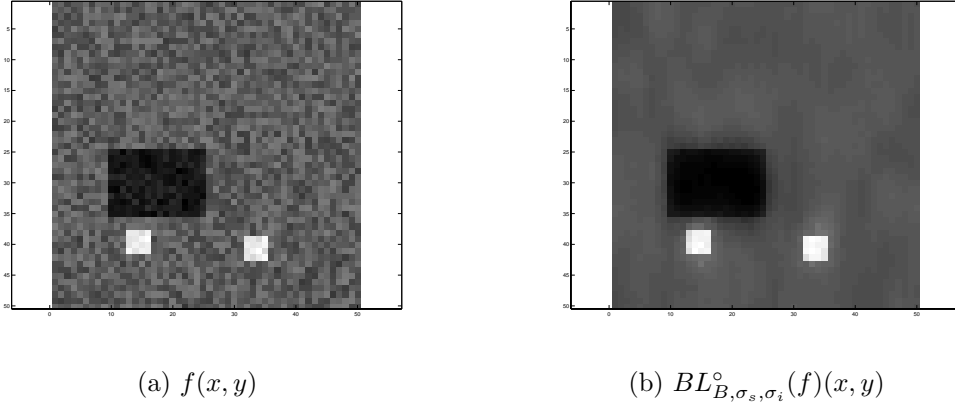


Figure 2.6: Noise reduction of original image (a) using the bilateral filter (b), with parameters $\sigma_s = 0.9$ and $\sigma_i = 0.9$ in a window B of size 5×5 pixels.

Weighted Fréchet mean results show a great improvement over regular Fréchet mean. It is an useful tool to remove noise, as illustrated in Fig. 2.6. But it does not make any better when applied to erosion and dilation operators introduced further below.

2.3.1 Trilateral filtering

If a prior information about the data is available, detecting a specific type of known target can be required. Let us consider that the “target” has a particular distribution of values on the sphere. This is formed by a set of points characterized with its mean and variance: $\bar{\xi}_{ref}$ and $\sigma_{\xi_{ref}}^2$. For the purpose of denoising, appears reasonable to introduce a new weight component in the averaging that penalizes the points that have values far from the intended target values.

Indeed, we can combine by product the coefficients of the bilateral filter, with the ones obtained from the distance between the pixel and the mean of the target set $\bar{\xi}_{ref}$. The *Fréchet*

trilateral filter on the sphere of image $f(x, y) \in \mathcal{F}(E, \mathbb{S}^2)$ adapted to target of mean value $\bar{\xi}_{ref}$ given by:

$$TL_{B, \sigma_s, \sigma_i, \sigma_r}^{\circ, \bar{\xi}_{ref}}(f)(x, y) = \left\{ \mu_{\sigma_s, \sigma_i, \sigma_r}^{\circ, \bar{\xi}_{ref}}([f(v, w)]); (v, w) \in B(x, y) \right\}$$

where $\mu_{\sigma_s, \sigma_i, \sigma_r}^{\circ, \bar{\xi}_{ref}}$ is the weighted Fréchet mean using the trilateral weights given by

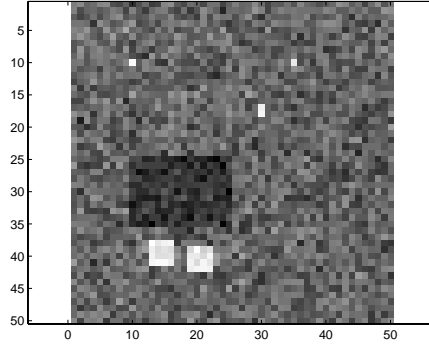
$$W_{\sigma_s, \sigma_i, \sigma_r}^{\bar{\xi}_{ref}}(u, v) = \frac{1}{\widetilde{W}^{\bar{\xi}_{ref}}(x, y)} e^{-\frac{(x-u)^2 + (y-u)^2}{2\sigma_s^2}} e^{-\frac{-d(f(u, v), f(x, y))^2}{2\sigma_i^2}} e^{-\frac{-d(f(u, v), \bar{\xi}_{ref})^2}{2\sigma_r^2}} \quad (2.11)$$

and the normalization factor

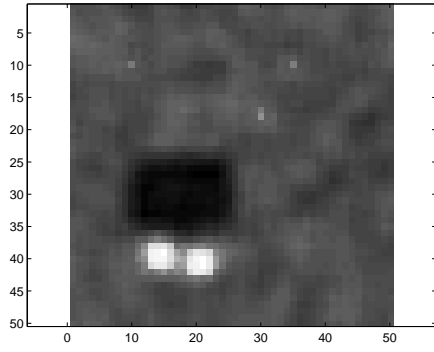
$$\widetilde{W}^{\bar{\xi}_{ref}}(x, y) = \sum_{(u, v) \in B(x, y)} e^{-\frac{(x-u)^2 + (y-u)^2}{2\sigma_s^2}} e^{-\frac{-d(f(u, v), f(x, y))^2}{2\sigma_i^2}} e^{-\frac{-d(f(u, v), \bar{\xi}_{ref})^2}{2\sigma_r^2}}$$

The key parameter to optimize here, in order to preserve the small targets but simultaneously denoise the image, is the dispersion used for computing the coefficient associated to the reference, i.e., σ_r . In fact, this parameter is related to the variance of the target values $\sigma_{\xi_{ref}}^2$ and a more deeper study on the question is required to conclude about the appropriate approach for tuning this parameter.

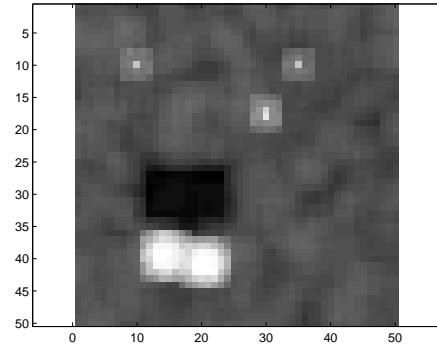
As it is illustrated in Fig. 2.7, the (unsupervised) bilateral filter set out above are not sufficient to enhance small targets, often hidden by noise. This supervised trilateral method brings off better results losing resolution in the images.



(a) $f(x, y)$



(b) $BL_{B, \sigma_s, \sigma_i}^\circ(f)(x, y)$



(c) $TL_{B, \sigma_s, \sigma_i, \sigma_r}^{\circ, \bar{\xi}_{ref}}(f)(x, y)$

Figure 2.7: When the targets to be detected are small in the original image (a), the trilateral filter adapted to this particular targets achieves better performance (c) than bilateral filter (b).

Chapter 3

Short review on morphological operators for scalar images

Mathematical morphology is a well-known nonlinear image processing methodology based on the application of lattice theory to spatial structures [21, 22] [12] [25].

The aim of this chapter is to provide a background on the basic morphological operators for scalar images. This short review is necessary to fix the notation and to make easier the definition of the new operators for images valued on \mathbb{S}^2 .

3.1 Scalar images

Let E be a subset of the Euclidean \mathbb{R}^d or the discrete space \mathbb{Z}^d , considered as the *support space* of the image, and let \mathcal{T} be a set of grey-levels, corresponding to the *space of values* of the image. It is assumed that $\mathcal{T} = \overline{\mathbb{R}} = \mathbb{R} \cup \{-\infty, +\infty\}$. A grey-level image is represented by a function,

$$f : \begin{cases} E & \rightarrow \mathcal{T} \\ \mathbf{x} & \mapsto t \end{cases} \quad (3.1)$$

i.e., $f \in \mathcal{F}(E, \mathcal{T})$ maps each pixel $\mathbf{x} \in E$ into a grey-level value $t \in \mathcal{T}$: $t = f(\mathbf{x})$.

3.2 Dilation and erosion

The two basic morphological mappings $\mathcal{F}(E, \mathcal{T}) \rightarrow \mathcal{F}(E, \mathcal{T})$ are the *grey-level dilation* and the *grey-level erosion* given respectively by

$$\delta_b(f)(\mathbf{x}) = \sup_{\mathbf{h} \in E} (f(\mathbf{x} - \mathbf{h}) + b(\mathbf{h})) \quad (3.2)$$

and

$$\varepsilon_b(f)(\mathbf{x}) = \inf_{\mathbf{h} \in E} (f(\mathbf{x} + \mathbf{h}) - b(\mathbf{h})), \quad (3.3)$$

where $f \in \mathcal{F}(E, T)$ is the original grey-level image and $b \in \mathcal{F}(E, T)$ is the fixed *structuring function*. The further convention for ambiguous expression is considered: $f(\mathbf{x} - \mathbf{h}) + b(\mathbf{h}) = -\infty$ when $f(\mathbf{x} - \mathbf{h}) = -\infty$ or $b(\mathbf{h}) = -\infty$, and that $f(\mathbf{x} + \mathbf{h}) - b(\mathbf{h}) = +\infty$ when $f(\mathbf{x} + \mathbf{h}) = +\infty$ or $b(\mathbf{h}) = -\infty$.

Particularly interesting in theory and in practical applications [25], the flat grey-level dilation and erosion is obtained when the structuring function is flat and becomes a *structuring element*. More precisely, a flat structuring function of support subspace B is defined as

$$b(\mathbf{x}) = \begin{cases} 0 & \mathbf{x} \in B \\ -\infty & \mathbf{x} \in B^c \end{cases},$$

where B is a Boolean set, *i.e.*, $B \subseteq E$ or $B \in \mathcal{P}(E)$, which defines the “shape” of the structuring element. We notice that B^c denotes the complement set of B (*i.e.*, $B \cap B^c = \emptyset$ and $B \cup B^c = E$). The structuring element is defined at the origin $\mathbf{o} \in E$, then to each point \mathbf{p} of E corresponds the translation mapping \mathbf{o} to \mathbf{p} , and this translation maps B onto $B_{\mathbf{p}}$, *i.e.*, $B_{\mathbf{p}} = \{\mathbf{b} + \mathbf{p} : \mathbf{b} \in B\}$. Therefore, the *flat dilation and erosion of a grey-level image* $f(\mathbf{x})$ with respect to the structuring element B are respectively

$$\begin{aligned} \delta_B(f)(\mathbf{x}) &= \sup_{\mathbf{h} \in B} (f(\mathbf{x} - \mathbf{h})) \\ &= \{f(\mathbf{y}) \mid f(\mathbf{y}) = \sup[f(\mathbf{z})], \mathbf{z} \in B_{\mathbf{x}}\} \end{aligned} \quad (3.4)$$

and

$$\begin{aligned} \varepsilon_B(f)(\mathbf{x}) &= \inf_{\mathbf{h} \in B} (f(\mathbf{x} + \mathbf{h})) \\ &= \{f(\mathbf{y}) \mid f(\mathbf{y}) = \inf[f(\mathbf{z})], \mathbf{z} \in \check{B}_{\mathbf{x}}\}, \end{aligned} \quad (3.5)$$

where \check{B} is the *reflection* of B with respect to the origin, *i.e.*, $\check{B} = \{-\mathbf{b} \mid \mathbf{b} \in B\}$. Dilation and erosion are dual operators with respect to the image complement (negative), *i.e.*,

$$\delta_B(f) = (\varepsilon_B(f^c))^c$$

where $f^c(\mathbf{x}) = -f(\mathbf{x})$. Dilation and erosion are increasing operators: if $f \leq g$, $\forall \mathbf{x} \in E$, then $\delta_B(f) \leq \delta_B(g)$ and $\varepsilon_B(f) \leq \varepsilon_B(g)$, $\forall \mathbf{x} \in E$. Dilation (erosion) is an extensive (anti-extensive) operator, *i.e.*, $f \leq \delta_B(f)$ ($\varepsilon_B(f) \leq f$), $\forall \mathbf{x} \in E$, when the structuring element B contains the origin. The two following properties also hold:

- Distributivity:

$$\begin{aligned} \delta_B(f \bigvee g)(\mathbf{x}) &= \delta_B(f)(\mathbf{x}) \vee \delta_B(g)(\mathbf{x}) \\ \varepsilon_B(f \bigwedge g)(\mathbf{x}) &= \varepsilon_B(f)(\mathbf{x}) \wedge \varepsilon_B(g)(\mathbf{x}) \end{aligned}$$

- Associativity:

$$\begin{aligned} \delta_{B_2}(\delta_{B_1}(f))(\mathbf{x}) &= \delta_{B_1 \oplus B_2}(f)(\mathbf{x}) \\ \varepsilon_{B_2}(\varepsilon_{B_1}(f))(\mathbf{x}) &= \varepsilon_{B_1 \oplus B_2}(f)(\mathbf{x}) \end{aligned}$$

where $B_1 \oplus B_2$ is the Minkowski addition of the structuring elements.

3.3 Opening and closing

The two elementary operations of grey-level erosion and dilation can be composed together to yield a new set of grey-level operators having desirable feature extractor properties which are the opening and the closing. More precisely, starting from the adjunction pair $\{\delta_b, \varepsilon_b\}$, the *opening and closing of a grey-level image f* according to the structuring function b are the mappings $\mathcal{F}(E, \mathcal{T}) \rightarrow \mathcal{F}(E, \mathcal{T})$ given respectively by

$$\gamma_b(f)(\mathbf{x}) = [\delta_b(\varepsilon_b(f))](\mathbf{x}), \quad (3.6)$$

and

$$\varphi_b(f)(\mathbf{x}) = [\varepsilon_b(\delta_b(f))](\mathbf{x}). \quad (3.7)$$

The flat counterparts are obtained by using the flat erosion and flat erosion by the structuring element B . The opening and closing are dual operators, i.e.,

$$\gamma_B(f) = (\varphi_B(f^c))^c$$

Opening (closing) removes positive (negative) structures according to the predefined size and shape criterion of the structuring element B : they smooth in a nonlinear way the image.

The pair (γ_B, φ_B) is called adjunction opening and adjunction closing. Let $f, g \in \mathcal{F}(E, \mathcal{T})$ be two grey-level images. The opening γ_B and closing φ_B verify the following properties.

- Increasingness (ordering preservation): γ_B and φ_B are increasing as products of increasing operators, i.e., $f(\mathbf{x}) \leq g(\mathbf{x}) \Rightarrow \gamma_B(f)(\mathbf{x}) \leq \gamma_B(g)(\mathbf{x}), \varphi_B(f)(\mathbf{x}) \leq \varphi_B(g)(\mathbf{x})$.
- Idempotence (invariance with respect to the transformation itself): γ_B and φ_B are idempotent, i.e., $\gamma_B(\gamma_B(f)) = \gamma_B(f), \varphi_B(\varphi_B(f)) = \varphi_B(f)$.
- Extensivity and anti-extensivity: γ is anti-extensive, i.e., $\gamma_B(f)(\mathbf{x}) \leq f(\mathbf{x})$; and φ is extensive, i.e., $f(\mathbf{x}) \leq \varphi_B(f)(\mathbf{x})$.

The other morphological operators are obtained as products of openings/closings or by residues between erosion/dilation and opening/closing.

Chapter 4

Morphological residues-based on distances as target detectors

Some other morphological operators obtained combining erosion and dilation are explained below. These are widely used to detect objects as regions rather homogeneous. Either we can display the contours of the objects, or extract image structures for a given structuring element shape.

4.1 Nonlinear-gradient based on distances

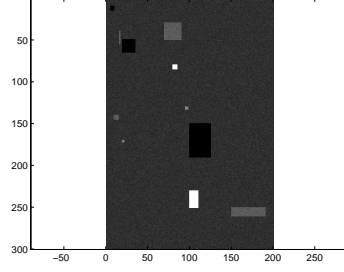
Gradient operators enhance intensity variations in images, in order to detect object boundaries. The gradient calculus is based on the difference between dilations and erosions, or more generally between anti-extensive transformations.

$$g_B(f)(x, y) = \delta_B(f)(x, y) - \varepsilon_B(f)(x, y) \quad (4.1)$$

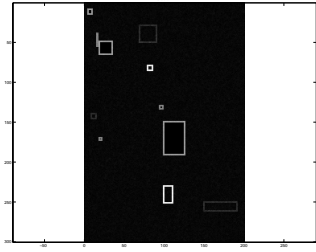
where B describes an structuring element centered on x and δ and ε are dilation and erosion respectively. It has been showed in [11] that the operator behavior differs when applied to image data distributed on the unit circle. The expression (4.1) can be rewritten according to the following relation

$$g_B^\circ(f)(x, y) = \bigvee_{\substack{(u, v) \in B(x, y) \\ (u, v) \neq (x, y)}} d(f(x, y), f(u, v)) - \bigwedge_{\substack{(u, v) \in B(x, y) \\ (u, v) \neq (x, y)}} d(f(x, y), f(u, v)) \quad (4.2)$$

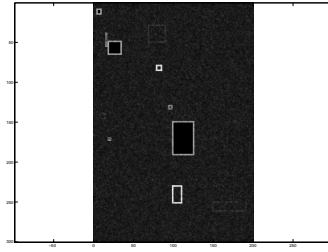
with \bigvee and \bigwedge the supremum and infimum respectively and $d(f(x, y), f(u, v))$ can be replaced with the corresponding metric. In the case of interest, the exposed concepts are extended to the unit sphere, where the distance measure used is the geodesic distance of \mathbb{S}^2 . Note that the resulting image is a grey-level escalar image, ie. it has only one component.



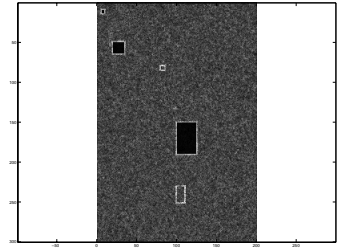
(a) $f_1(x, y)$



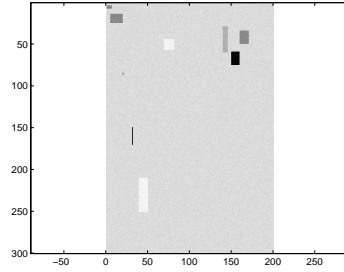
(b) $g_B^{\circ}(f_1)(x, y)$ $\sigma = 0.1$



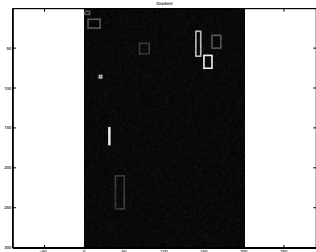
(c) $g_B^{\circ}(f_1)(x, y)$ $\sigma = 0.3$



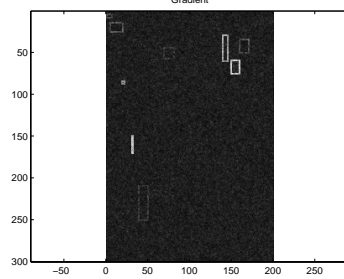
(d) $g_B^{\circ}(f_1)(x, y)$ $\sigma = 1$



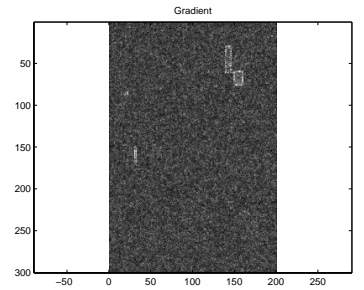
(e) $f_2(x, y)$



(f) $g_B^{\circ}(f_2)(x, y)$ $\sigma = 0.1$



(g) $g_B^{\circ}(f_2)(x, y)$ $\sigma = 0.3$



(h) $g_B^{\circ}(f_2)(x, y)$ $\sigma = 1$

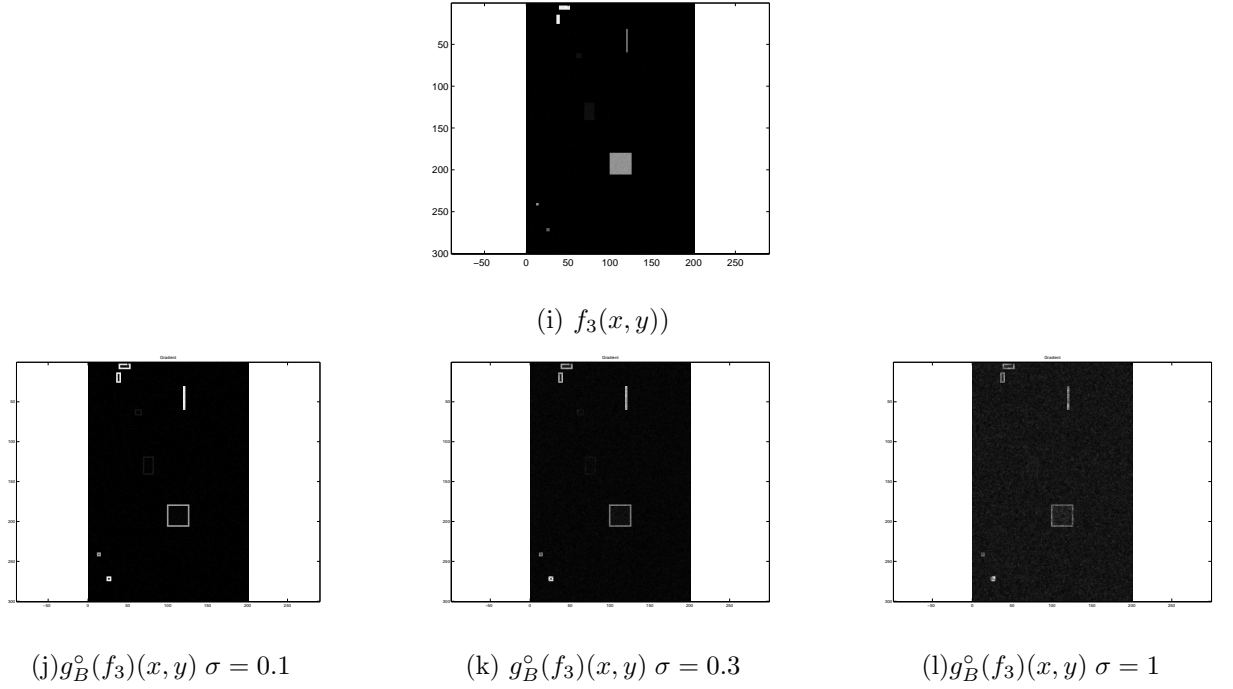


Figure 4.1: Original images (a),(e),(i), (first coordinate on \mathbb{S}^2). Morphological gradient for three different noise levels $\sigma = 0.1, \sigma = 0.3$ and $\sigma = 1$, with B a square of size 3×3 .

4.2 Top-hat based on distances

The Top-hat operators extract all contrasted components that can not contain the structuring element (ie. peaks and troughs). Three different formulations are found in literature:

- The *white Top-hat* is the residue between the original image f and its opening γ .

$$\rho_B^+(f)(x, y) = f(x, y) - \gamma_B(f)(x, y) \quad (4.3)$$

and it extracts positive components.

- The *black Top-hat* is defined as the difference between the closing φ of the original image and the original image

$$\rho_B^-(f)(x, y) = \varphi_B(f)(x, y) - f(x, y) \quad (4.4)$$

it extracts the negative components.

- The *self-complementary Top-hat* is the sum of the white and black Top-hats. It leads to the difference between the closing and the opening of the image.

$$\rho = \rho^+ + \rho^- = \varphi - \gamma \quad (4.5)$$

According to [11] it involves only increments and then the expression (4.5) can be rewritten as

$$\rho_B^\circ(f)(x, y) = \bigvee_{(u,v) \in B(x,y)} -\mathcal{V}_B^\circ(u, v) \quad (4.6)$$

where

$$\mathcal{V}_B^\circ(x, y) = \bigwedge_{(u,v) \in B(x,y)} -d(f(x, y), f(u, v))$$

And in this particular case $d(f(x, y), f(u, v))$ corresponds to the Riemannian distance on \mathbb{S}^2 . Top-hat operator also leads to a grey-level escalar image.

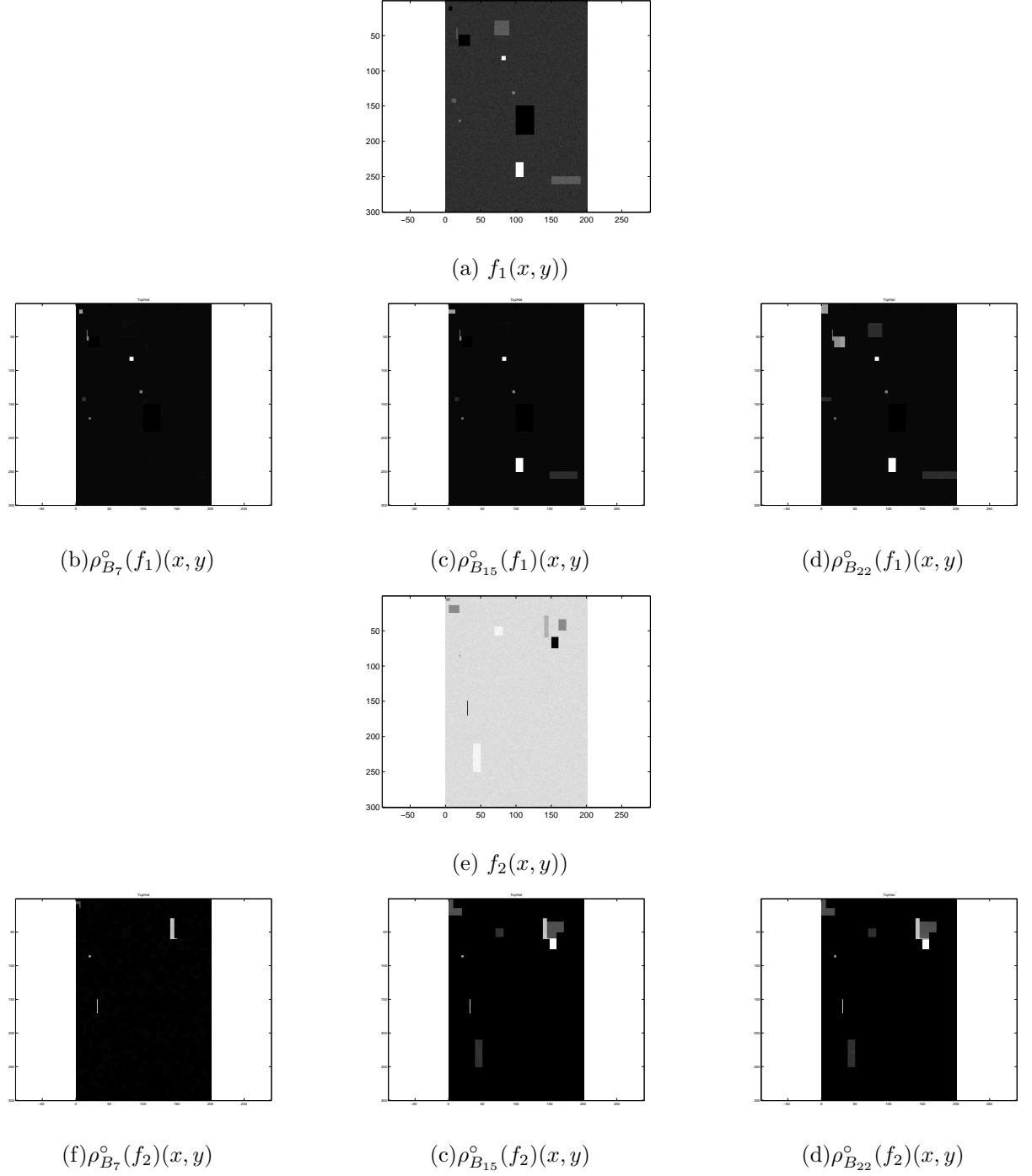


Figure 4.2: *Self-complementary Top-Hat* for three different sizes of the structuring element B .

4.3 Application to target detection

For target detection purposes we intend to identify zones strong contrasted with the clutter. Gradient is an useful operator to detect the edges of the objects. While top-hat extracts highly contrasted structures smaller than the structuring element. The problem is that they are very sensitive to noise. ROC curves depict the performance of the operators, thresholding values for different detection levels. Fig. 4.3 reveals the great improvement introduced by a pre-filtering stage using the filters described in chapter chapter2. Third image achieves better results because the different objects in the image are located far apart from each other on the sphere.

The morphological operators based on residues can be generalized to \mathbb{S}^2 replacing the grey-level difference by the distance on the sphere. This is limited to a few operators. Below in the document, we propose several generalizations of dilation and erosion, such that the morphological operators could be completely defined on the sphere.

CHAPTER 4. MORPHOLOGICAL RESIDUES-BASED ON DISTANCES AS TARGET DETECTORS

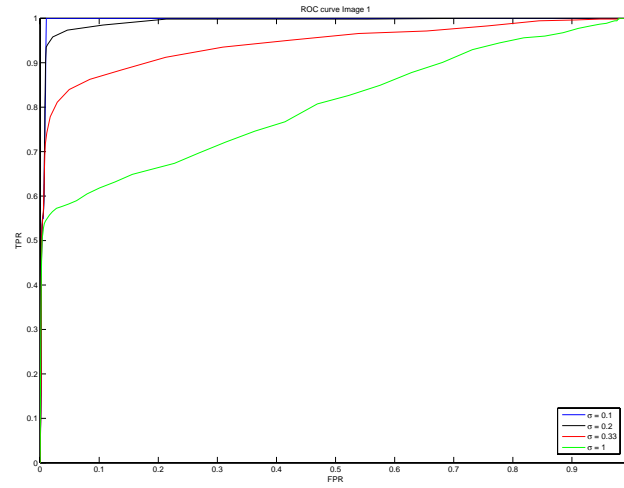
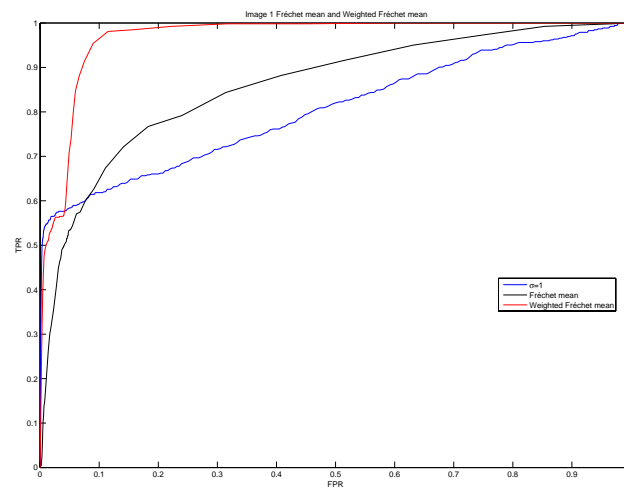


Image $f_{1,\sigma_i}(x, y)$



Filtered image $f_{1,\sigma=1}(x, y)$

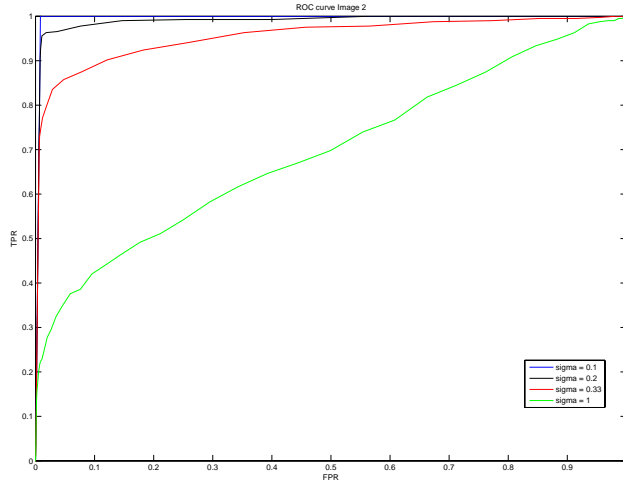
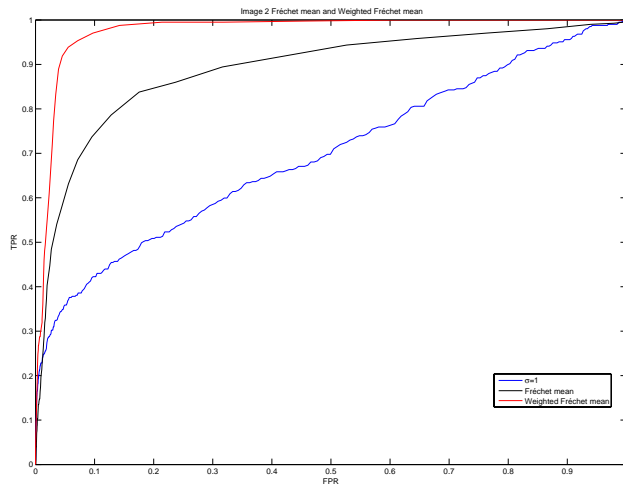


Image $f_{2,\sigma_i}(x, y)$



Filtered image $f_{2,\sigma=1}(x, y)$

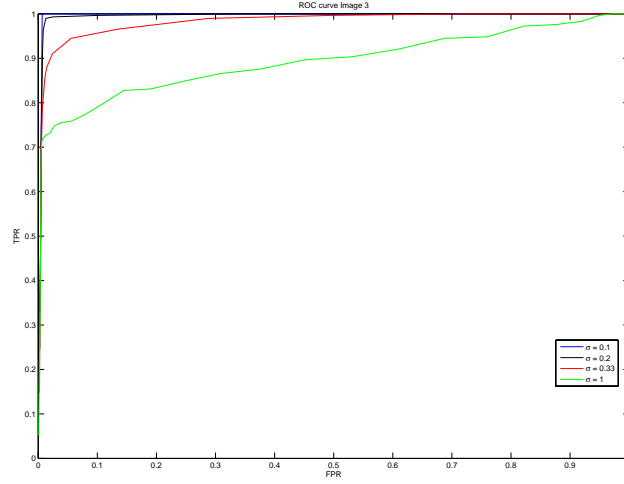
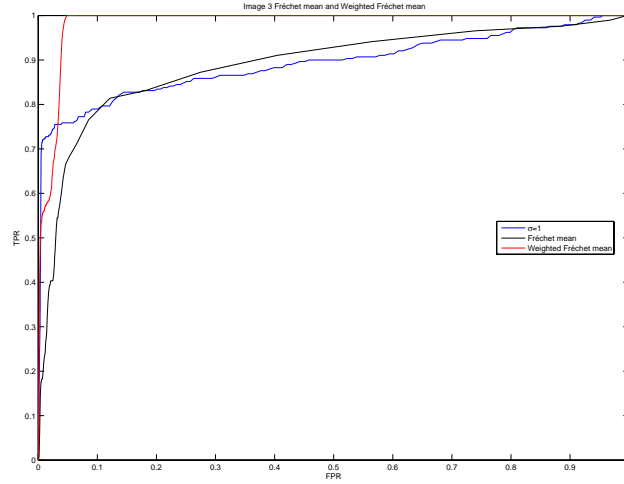


Image $f_{2,\sigma_i}(x, y)$



Filtered image $f_{3,\sigma=1}(x, y)$

Figure 4.3: ROC curves representing the performance of the gradient for different noise levels. For $\sigma = 1$ the different filters results are compared.

Chapter 5

Supremum and infimum on \mathbb{S}^2

This chapter deals with a formulation of partial ordering indicated when the data set is embedded on the sphere surface. In particular, we develop two algorithms to determine supremum and infimum values for a set of points lying on \mathbb{S}^2 . They are applied to the corresponding sup and inf operators found in the definitions of dilation and erosion, which lead to pseudo-dilation and pseudo-erosion \mathbb{S}^2 . Other evolved morphological operators are studied considering this new approach.

5.1 Local origin on the sphere and supremum/infimum computation on tangent space

Computation of the supremum and infimum of a set of points requires defining an ordering relationship between them. It is obvious that there is no natural ordering on the sphere. In fact, the sphere is probably one of the more complex geometrical objects for the notion of ordering and consequently for the computation of supremum and infimum values.

The notion of supremum in vectorial spaces is usually associated to a marginal computation of maximum coordinates, which involves also a value which has maximal Euclidean distance to the origin. The latter considered as the smallest element of the space. A possible solution to deal with \mathbb{S}^2 will consist just in defining a local origin on the sphere and try after projecting on the tangent space, compute a vectorial-like supremum.

This is the idea which introduced in this section. The approach induces a partial ordering “adapted” to a particular set of values on the sphere, and it is related to the definition of a barycenter, which allows defining a local Euclidean coordinate system.

5.1.1 Supremum

Let $R = \{\xi_i\}_{i=1}^N$ be a set of points lying on the sphere surface. First, the Fréchet mean of the set is computed, as explained in Section 2.2:

$$\bar{\xi} = \mu^\circ(R) \quad (5.1)$$

Considering this center as the origin of R , we use it to carry out a rotation on \mathbb{S}^2 of each point belonging to the set R . The barycenter is moved to the “north pole”, $\mathbf{N} = (0, 0, 1)$, and this translation completely describes the axis and the angle needed to determine the rotation matrix $\mathcal{M}_{\mathbf{N}}(\bar{\xi})$, which is then applied to all the points for the points of R :

$$\xi_i \mapsto \tilde{\xi}_i = \mathcal{M}_{\mathbf{N}}(\bar{\xi}) \cdot \xi_i^T \quad \forall \xi_i \in R \quad (5.2)$$

where T is the transpose operator and \sim indicates the locations once rotated. Therefore, all $\tilde{\xi}_i \in \tilde{R}$ and $\tilde{\xi} = (0, 0, 1)$, the previously computed Fréchet mean, are placed around \mathbf{N} , preserving the same configuration they had, see Fig. 5.1(a)-(b).

Next step, all $\tilde{\xi}_i \in \tilde{R}$ will be projected to the space tangent at \mathbf{N} , denoted $T_{\mathbf{N}}\mathbb{S}^2$, using the expression referred in Eq. (2.4). Let us denote by $\vec{\nu}_i = (\nu_{1,i}, \nu_{2,i}, \nu_{3,i})$ are the projected points on $T_{\mathbf{N}}\mathbb{S}^2$:

$$\vec{\nu}_i = \exp_{\tilde{\xi}}^{-1}(\tilde{\xi}_i) \quad (5.3)$$

Thus, having $\mathbf{N} = (0, 0, 1)$ as the projection point leads to a tangent plane contained in \mathbb{R}^2 , i.e., $T_{\mathbf{N}}\mathbb{S}^2 \subset \mathbb{R}^2$ such that $\nu_{3,j} = 0, \forall j$.

The smallest box that may contain these points in $T_{\mathbf{N}}\mathbb{S}^2$ is defined by its four corners, obtained as the minimum and maximum values of each of the coordinates for both axes, and the combinations between them, i.e., $\vee \nu_{1,i}, \wedge \nu_{1,i}$ and $\vee \nu_{2,i}, \wedge \nu_{2,i}$, see Fig. 5.2. We consider these four points as the four candidates to calculate the supremum:

$$\vec{\nu}_{sup} \in \{\vec{\nu}_1^\square = (\vee \nu_{1,i}, \vee \nu_{2,i}), \vec{\nu}_2^\square = (\wedge \nu_{1,i}, \wedge \nu_{2,i}), \vec{\nu}_3^\square = (\vee \nu_{1,i}, \wedge \nu_{2,i}), \vec{\nu}_4^\square = (\wedge \nu_{1,i}, \vee \nu_{2,i})\} \quad (5.4)$$

Then, we select as supremum the one furthest from $\tilde{\xi}$. As $\tilde{\xi}$ in tangent space $T_{\mathbf{N}}\mathbb{S}^2$ corresponds to the origin $(0, 0)$, it is equivalent to say that $\vec{\nu}_{sup}$ is the corner of the box having the largest norm, i.e.,

$$\vec{\nu}_{sup} = \arg \max_{j=1, \dots, 4} \|\vec{\nu}_j^\square\| \quad (5.5)$$

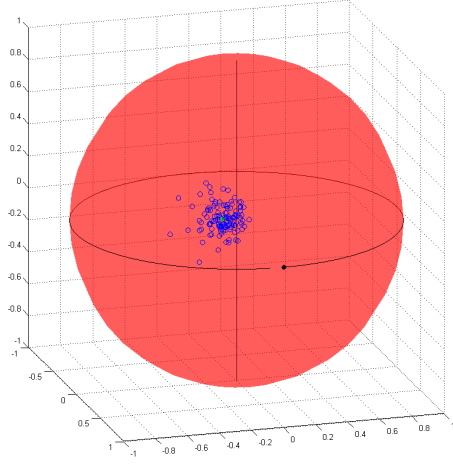
Now, $\vec{\nu}_{sup}$ is projected back to the sphere, according to Eq. (2.5):

$$\tilde{\xi}_{sup} = \exp_{\tilde{\xi}}(\vec{\nu}_{sup}) \quad (5.6)$$

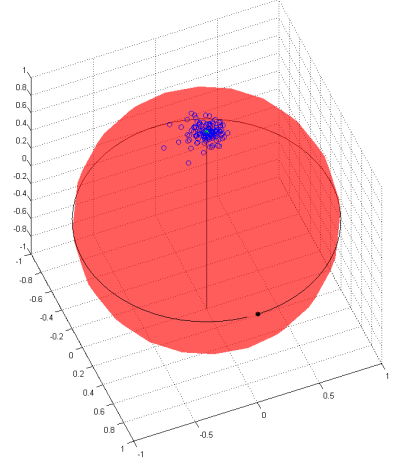
and finally moved to its original polarization states by reversing the rotation:

$$\sup_{\bar{\xi}} [\{\xi_i\}_{i=1}^N] = \mathcal{M}_{\mathbf{N}}(\bar{\xi})^T \cdot \tilde{\xi}_{sup}^T \quad (5.7)$$

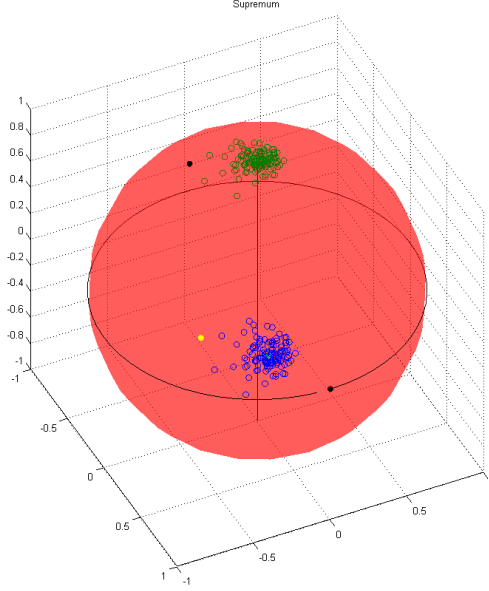
An example of these two last steps is given in Fig. 5.1(c).



(a)



(b)



(c)

Figure 5.1: Figure (a) shows the original set R , and its Fréchet mean in green. Figure (b) is the result of the rotation of the set to \mathbf{N} . Figure (c) illustrates how $\vec{\nu}_{sup}$ is projected back to the sphere and the rotation is reversed, in yellow the value of the supremum.

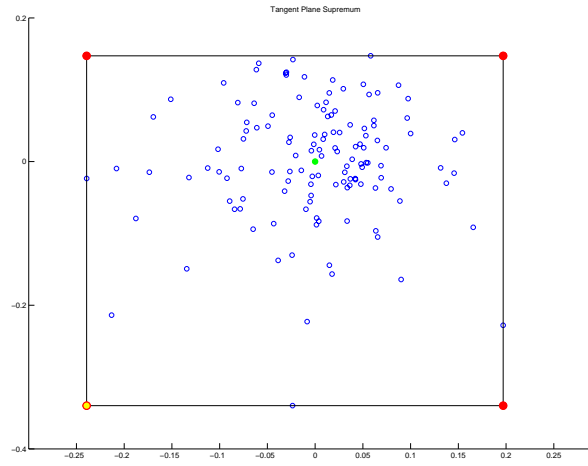


Figure 5.2: Tangent plane $T_{\mathbf{N}}\mathbb{S}^2$, with all the projected points \vec{v}_i . We note that $\tilde{\tilde{\xi}}$, in green, is found at the origin. The red dots are the four candidates \vec{v}_j^{\square} , $j = 1, \dots, 4$, and the yellow one is the furthest from the origin \vec{v}_{sup} .

5.1.2 Infimum

The method proposed to calculate the infimum is similar to the one presented for the supremum. In fact, we will introduce a duality in $T_{\mathbf{N}}\mathbb{S}^2$ which is associated to the inversion of coordinates.

We start by same steps as for the supremum: after computing the Fréchet mean Eq.(5.1), and performing the rotation of the set Eq.(5.2), all $\tilde{\xi}_i \in \tilde{R}$ are projected to the plane tangent at \mathbf{N} using Eq.(5.3).

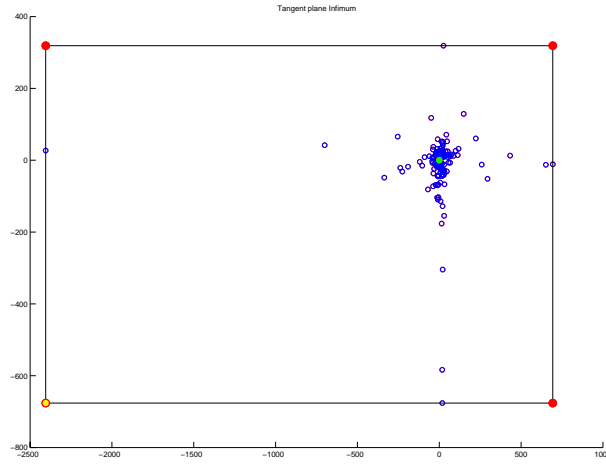


Figure 5.3: Inverted plane from tangent plane $T_{\mathbf{N}}\mathbb{S}^2$. The points are displayed once their coordinates have been inverted, $\vec{\theta}_i, \tilde{\xi}$ in green is found at the origin (without inversion since its inversion correspond to the infinity). The four red dots are the candidates to infimum and in yellow, the chosen one.

Now, the coordinates of each $\vec{\nu}_i$ lying on $T_{\mathbf{N}}\mathbb{S}^2$ are inverted to obtain a set of point given by

$$\vec{\theta}_i = \left(\frac{1}{\nu_{1,i}}, \frac{1}{\nu_{2,i}}, 0 \right) \quad (5.8)$$

Computing the maximum and minimum for inverted coordinates $\theta_{1,i}$ and $\theta_{2,i}$, $i = 1 \dots N$, it is obtained, as for the supremum, the four candidates to the infimum:

$$\vec{\theta}_{inf} \in \{\bar{\theta}_1^\square, \bar{\theta}_2^\square, \bar{\theta}_3^\square, \bar{\theta}_4^\square\} \quad (5.9)$$

where

$$\begin{aligned} \bar{\theta}_1^\square &= \left(\bigvee \frac{1}{\nu_{1,i}}, \bigvee \frac{1}{\nu_{2,i}} \right), & \bar{\theta}_2^\square &= \left(\bigwedge \frac{1}{\nu_{1,i}}, \bigwedge \frac{1}{\nu_{2,i}} \right) \\ \bar{\theta}_3^\square &= \left(\bigvee \frac{1}{\nu_{1,i}}, \bigwedge \frac{1}{\nu_{2,i}} \right), & \bar{\theta}_4^\square &= \left(\bigwedge \frac{1}{\nu_{1,i}}, \bigvee \frac{1}{\nu_{2,i}} \right) \end{aligned}$$

and the one furthest from the Fréchet mean is chosen:

$$\vec{\theta}_{inf} = \arg \max_{j=1,\dots,4} \|\vec{\theta}_j^\square\| \quad (5.10)$$

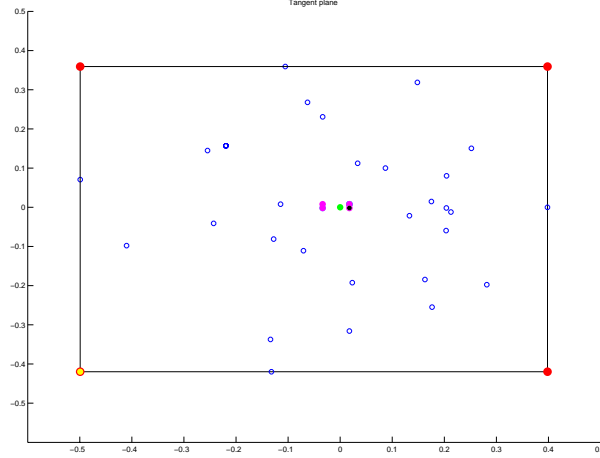


Figure 5.4: Tangent plane $T_{\mathbf{N}}\mathbb{S}^2$. The four red dots are the four candidates for the supremum $\vec{\nu}_j^\square$, $j = 1, \dots, 4$, and the yellow is the furthest from the origin $\vec{\nu}_{sup}$. While the four dots in pink are the candidates for the infimum, obtained by inversion of $\vec{\theta}_j^\square$, $j = 1, \dots, 4$, and the black is the closest to the Fréchet mean $\vec{\nu}_{inf}$.

The coordinates of the point $\vec{\theta}_{inf}$ are reinverted to obtain the infimum in original tangent space $T_{\mathbf{N}}\mathbb{S}^2$:

$$\vec{\nu}_{inf} = \left(\frac{1}{\theta_{1,inf}}, \frac{1}{\theta_{2,inf}}, 0 \right)$$

and then, $\vec{\nu}_{inf}$ on $T_{\mathbf{N}}\mathbb{S}^2$ is projected back onto the sphere:

$$\tilde{\xi}_{inf} = \exp_{\bar{\xi}}(\vec{\nu}_{inf}) \quad (5.11)$$

In the last step, the infimum for R is obtained once the rotation is undone:

$$\inf_{\bar{\xi}} [\{\xi_i\}_{i=1}^N] = \mathcal{M}_{\mathbf{N}}(\bar{\xi})^T \cdot \tilde{\xi}_{inf}^T \quad (5.12)$$

An example of the computation of supremum and infimum in the tangent space $T_{\mathbf{N}}\mathbb{S}^2$ is given in Fig. 5.4.

As shown in Fig. 5.5 the value of the infimum is often close to the Fréchet mean, due to the fact that the points are highly concentrated around $\bar{\xi}$. It may happen that either $\nu_{1,i}$ or $\nu_{2,i}$ were zero, and so the coordinates could not be inverted, as illustrated in Fig. 5.6. In that case, the infimum value is decided to be the same value as the Fréchet mean.

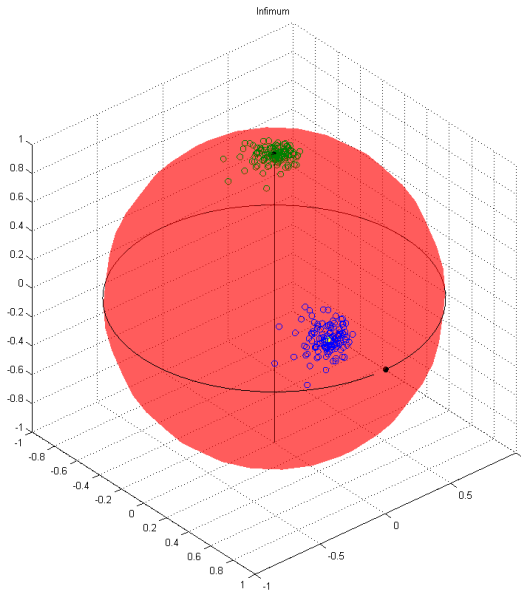


Figure 5.5: Computation of infimum for a set of points, including the result of projecting back to the sphere and undoing the rotation. In yellow the value of the infimum.

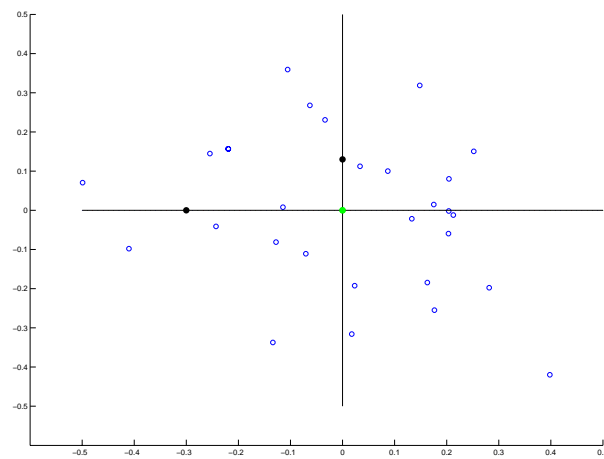


Figure 5.6: Case of computation of the infimum where the coordinates can not be inverted.

5.2 Pseudo-dilation and pseudo-erosion

In this section we extend the algorithms set forth to compute the supremum and the infimum, for the morphological erosion and dilation. Leading to a new formulation of these operators appropriate to the configuration of the data on typical images valued on the sphere.

5.2.1 Definition of sup/inf-based operators

As mentioned in Chapter 3, morphological flat dilation and erosion for grey-level images, $f \in \mathcal{F}(E, \mathbb{R})$ are defined

$$\delta_B(f)(x, y) = \{\sup [f(u, v)], (u, v) \in B(x, y)\} \quad (5.13)$$

and

$$\varepsilon_B(f)(x, y) = \{\inf [f(u, v)], (u, v) \in \check{B}(x, y)\}, \quad (5.14)$$

respectively.

Therefore, given an image valued on the sphere $f(x, y) \in \mathcal{F}(E, \mathbb{S}^2)$, we introduce the *flat pseudo-dilation on the sphere* as the operator defined by

$$\begin{cases} \delta_{W,B}^\circ(f)(x, y) = \left\{ \sup_{\bar{\xi}} [f(u, v) = \xi_j], (u, v) \in B(x, y) \right\} \\ \text{with } \bar{\xi} = \mu^\circ ([f(n, m) = \xi_i]), (n, m) \in W(x, y) \end{cases} \quad (5.15)$$

where B defines the shape of the structuring element and W is the window used for computing the Fréchet mean $\bar{\xi}$. Similarly, the *flat pseudo-erosion on the sphere* is defined by

$$\begin{cases} \varepsilon_{W,B}^\circ(f)(x, y) = \left\{ \inf_{\bar{\xi}} [f(u, v) = \xi_j], (u, v) \in \check{B}(x, y) \right\} \\ \text{with } \bar{\xi} = \mu^\circ ([f(n, m) = \xi_i]), (n, m) \in W(x, y) \end{cases} \quad (5.16)$$

5.2.2 Some properties and their use

A first remark concerning the name operators as pseudo-dilation/erosion. In fact, it is referred as “pseudo-dilation” (resp. “pseudo-erosion”) because, although its behavior is intuitively coherent with the dilation (resp. erosion) defined in Section 3.2, they are not fully equivalent. More precisely, the distributivity and associativity properties are not satisfied for the operators (5.15) and (5.16) described above. These limitations are well known for the “locally adaptive” operators [20]; we note that here the adaptability is appears in the computation of the local origin.

As discussed above, there is a notion of duality between the supremum and infimum.

From different tests, we have observed that the size of the window W should be larger than the structuring element B , and $B(x, y) \subset W(x, y)$ as they both have the same origin.

In fact, we need to use two different sizes to solve the instability of the Fréchet mean in neighborhoods near the edge of an object. Hence, the size of the window for the Fréchet mean computation is increased to make it more robust to the variability of the barycenter near edges. By this technique we can guarantee that the supremum/infimum for two close pixels is computed in the same tangent space, that is, the origin on the sphere will be the same. Note that the use of weighted Fréchet mean discussed in Chapter 2 will not introduce any improvement in the calculations of pseudo-dilation/erosion.

In Fig. 5.7 shows the results of pseudo-dilations and pseudo-erosions, using structuring elements of different size, for a simulated image $f(x, y) \in \mathbb{S}^2$. As we can observe, pseudo-dilations (resp. pseudo-erosions) increases (resp. reduces) the size of the objects since the local origin is generally the background for pixels close to the edges, and the value of the objects for pixels belonging to object.

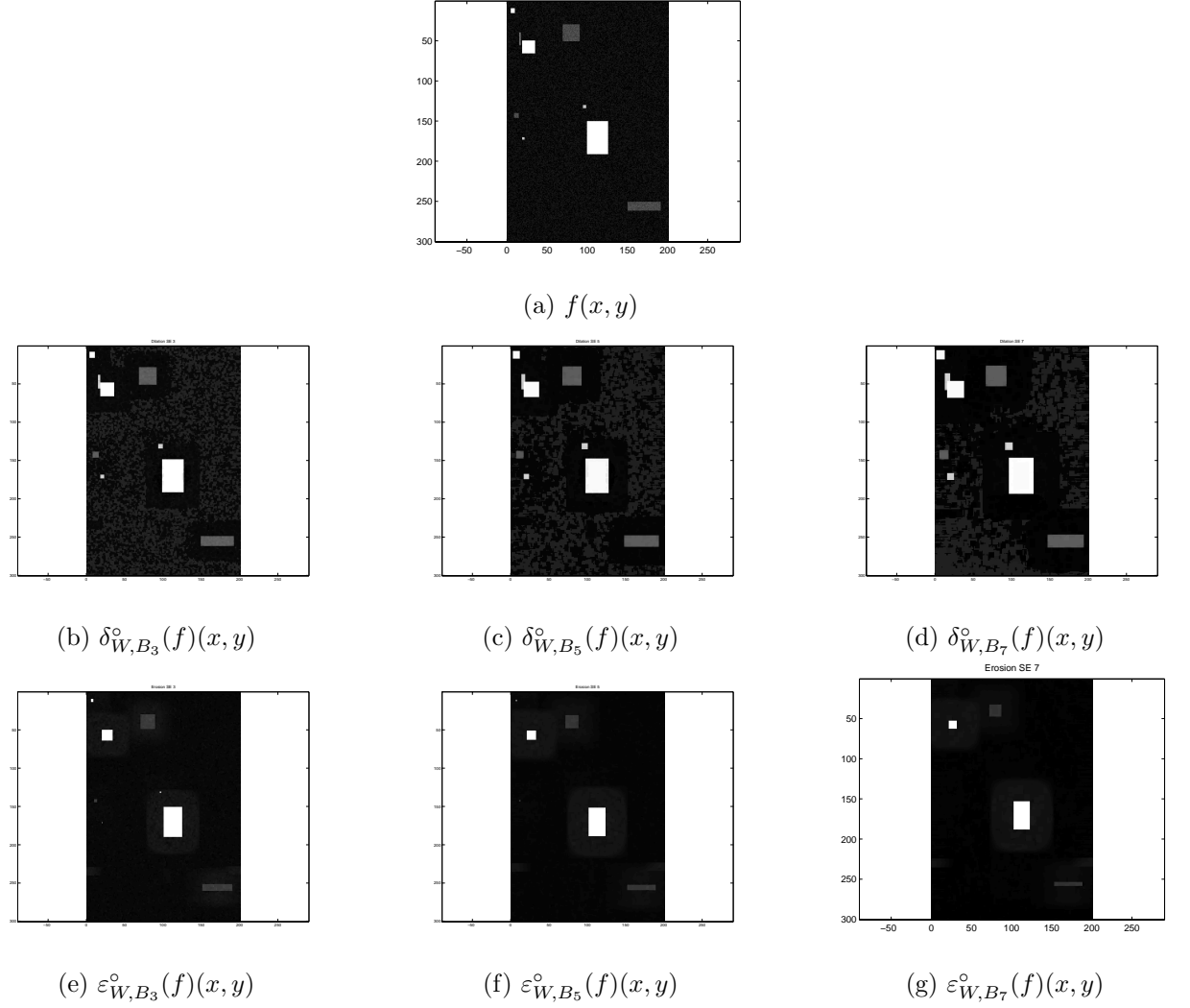


Figure 5.7: Examples of pseudo-dilation $\delta_{W, B_n}^\circ(f)(x, y)$ and pseudo-erosion $\varepsilon_{W, B_n}^\circ(f)(x, y)$ of image $f(x, y) \in \mathbb{S}^2$ in (a). The structuring element B_n is a square of size $n \times n$ pixels and W is a square of size \times . Note that in the Figures is shown only the image of the first coordinate on \mathbb{S}^2 .

5.3 Derived operators

Using the pseudo-dilation and pseudo-erosion on the sphere as basic bricks, other derived operators morphological can be extended to images valued on the sphere

5.3.1 Gradient on the sphere

As discussed above in the document, morphological gradient operator is obtained according to (4.1) as the difference between a flat dilation and a flat erosion using a structuring element B . Using the proposed formulations on the sphere for pseudo-dilation (5.15) and pseudo-erosion (5.16), we define the *morphological gradient on the sphere* of image $f \in \mathcal{F}(E, \mathbb{S}^2)$ as

$$g_{W,B}^\circ(f)(x, y) = d(\delta_{W,B}^\circ(f)(x, y), \varepsilon_{W,B}^\circ(f)(x, y)) \quad (5.17)$$

where $d(\xi_i, \xi_j)$ is the Riemannian distance on \mathbb{S}^2 .

Fig. 5.8 provides an example of the performance of the gradient operator, two different sizes of the structuring element are displayed.

5.3.2 Pseudo-opening and pseudo-closing on the sphere

In mathematical morphology, opening and closing are two key transformations for filtering purposes, as shown in Chapter 3 both derived from erosion and dilation by their direct products.

Now, using the proposed formulations on the sphere, we define the *flat pseudo-opening on the sphere* of image $f \in \mathcal{F}(E, \mathbb{S}^2)$ as the flat pseudo-dilation (5.15) applied on the pseudo-erosion (5.16) of original image f , i.e.,

$$\gamma_{W,B}^\circ(f) = \delta_{W,B}^\circ(\varepsilon_{W,B}^\circ(f)) \quad (5.18)$$

Similarly, the *flat pseudo-closing on the sphere* is defined as

$$\varphi_{W,B}^\circ(f) = \varepsilon_{W,B}^\circ(\delta_{W,B}^\circ(f)) \quad (5.19)$$

Some examples for pseudo-opening on the sphere shown in Fig. 5.9, using different structuring elements. The interpretation of these operators is exactly the same than for the opening/closing of grey-level images: opening removes objects from the foreground smaller than the structuring element and closing eliminates small holes in the background.

5.3.3 Top-hat on the sphere

Once the pseudo-opening and pseudo-closing on the sphere have been well-defined, we can also generalize the corresponding residue-based operators. Indeed the *white top-hat on the sphere* is the residue between the original image and its pseudo-opening transformation:

$$\rho_{W,B}^{+,\circ}(f)(x, y) = d(f(x, y), \gamma_{W,B}^\circ(f)(x, y)) \quad (5.20)$$

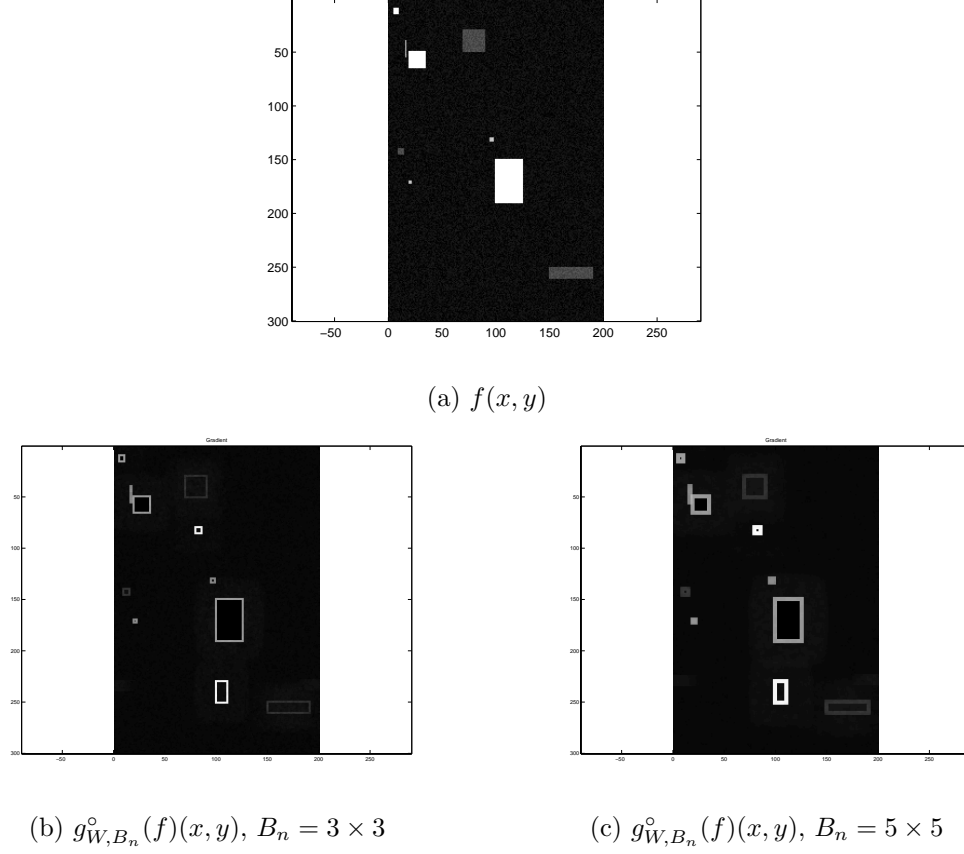


Figure 5.8: Examples of gradient $g_{W, B_n}^{\circ}(f)(x, y)$ of image $f(x, y) \in \mathbb{S}^2$. The image of the first coordinate on \mathbb{S}^2 of original image is given in (a). Note that the result of the gradient correspond to the scalar image given in (b) and (c).

and the *black top-hat on the sphere* is the residue between the original image and its pseudo-closing:

$$\rho_{W, B}^{-, \circ}(f)(x, y) = d(f(x, y), \varphi_{W, B}^{\circ}(f)(x, y)) \quad (5.21)$$

where, obviously, in both cases $d(\xi_i, \xi_j)$ is the Riemannian distance on \mathbb{S}^2 .

As for the grey-level case, the white (resp. black) top-hat allows extracting the image structures which have been removed by the opening (resp. the closing). For the examples given in Fig. 5.9, we observe that the white top-hat extract the targets of a particular scale, independently of their values on the sphere.

In the figures is shown only the image of the first coordinate on \mathbb{S}^2 for the original image and the dilations/erosion and the openings; however we should remark that the result top-hats $\rho_{W, B}^{+, \circ}(f)$ and $\rho_{W, B}^{-, \circ}(f)$ are scalar images. This is also the case for the gradient $g_{W, B}^{\circ}(f)(x, y)$.

5.3.4 Contrast on the sphere

The contrast mapping is a particular operator from a more general class of transformations called toggle mappings [23]. A contrast mapping is defined, on the one hand, by two primitives ϕ_1 and ϕ_2 applied to the initial function, and on the other hand, by a decision rule which makes, at each point (x, y) the output of this mapping toggles between the value of ϕ_1 at (x, y) and the value of ϕ_2 , according to which is closer to the input value of the function at (x, y) . If the primitives are an erosion and a dilation, the contrast mapping correspond to the shock filter [14]. This morphological transformation enhances the local contrast of the image by sharpening its edges. It is usually applied more than once, being iterated, and the iterations converge to a limit reached after a finite number of iterations.

Let us consider the generalization for the images $f(x, y) \in \mathcal{F}(E, \mathbb{S}^2)$. The *contrast on the sphere* using the pseudo-dilation and pseudo-erosion is the operators which returns the closest transformation value of the original image, i.e.,

$$\kappa_{W,B}^\circ(f)(x, y) = \begin{cases} \delta_{W,B}^\circ(f)(x, y) & \text{if } d\left(f(x, y), \delta_{W,B}^\circ(f)(x, y)\right) < d\left(f(x, y), \varepsilon_{W,B}^\circ(f)(x, y)\right) \\ \varepsilon_{W,B}^\circ(f)(x, y) & \text{if } d\left(f(x, y), \delta_{W,B}^\circ(f)(x, y)\right) > d\left(f(x, y), \varepsilon_{W,B}^\circ(f)(x, y)\right) \\ f(x, y) & \text{if } d\left(f(x, y), \delta_{W,B}^\circ(f)(x, y)\right) = d\left(f(x, y), \varepsilon_{W,B}^\circ(f)(x, y)\right) \end{cases} \quad (5.22)$$

where B is an unitary structuring elements.

The operator $\kappa_{W,B}^\circ(f)(x, y)$ provides interesting results when, after the trilateral filtering described in Section 2.3.1 the contours of the objects are blurry. Hence, if the goal is detecting small targets, the filtering stage removes the noise and contrast operator recover the edges. Fig. 5.10 illustrates just the performance of the contrast to create a highly contrasted signal after an averaging filter.

5.4 Conclusions and perspectives

We have explored in this chapter a first approach to the computation of supremum and infimum of a set of points on \mathbb{S}^2 , which is based on the notion of local origin to obtain the best tangent space where the supremum and infimum are computed as a vector notion. This methodology seems interesting from a practical viewpoint since the obtained morphological filters produce useful results.

However, there are many questions which should be explored in detail in subsequent studies. On the one hand, it should be proved that this local approach is more appropriate than a global one, typically computing the supremum and infimum in the space associated to the stereographic projection. On the other hand, there are some limited invariance properties of the supremum and infimum which are due to the computation in a rectangular box. It seems more interesting to consider a Euclidean ball (i.e., the supremum can be the point of the minimum enclosing ball which have the largest norm). It is necessary also to consider the

interest of defining the supremum (resp. infimum) as the center of the minimum enclosing disk (resp. of the maximum enclosed disk). A deeper study on the mathematical properties of these alternative pseudo-dilation and pseudo-erosion will be also required.

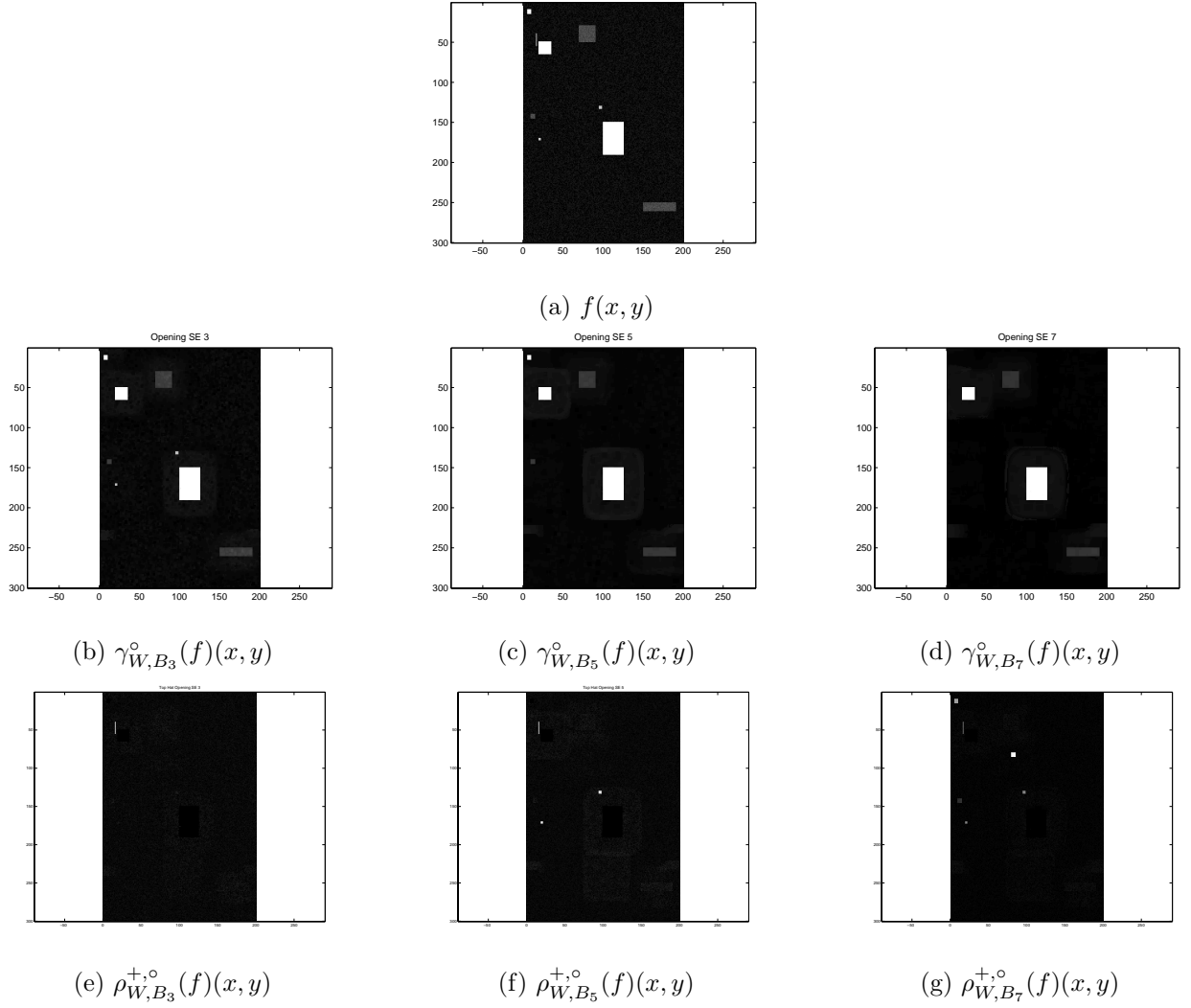
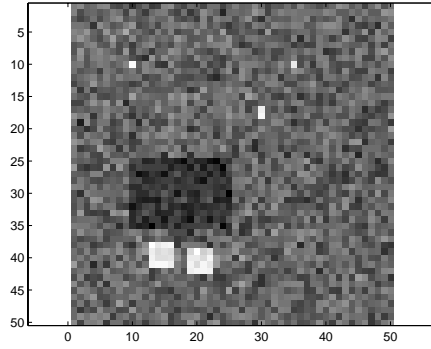
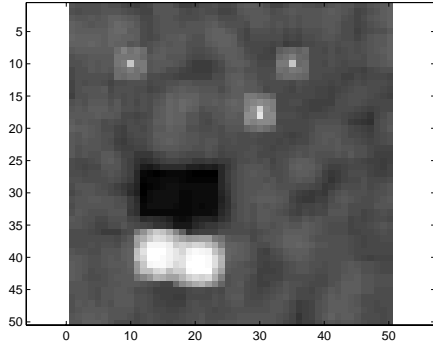


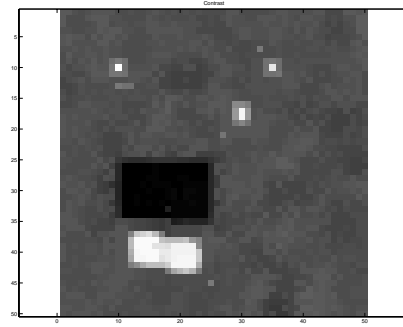
Figure 5.9: Examples of pseudo-opening $\gamma_{W, B_n}^\circ(f)(x, y)$ of image $f(x, y) \in \mathbb{S}^2$, given in (a), and its residue (top-hat) $\rho_{W, B_n}^{+, \circ}(f)(x, y)$. The structuring element B_n is a square of size $n \times n$ pixels and W is a square of size \times . Note that in the Figures (a)-(d) is shown only the image of the first coordinate on \mathbb{S}^2 , however for top-hat images, the result is the given scalar image.



(a) $f(x, y)$



(b) $f_1(x, y) = TL_{B, \sigma_s, \sigma_i, \sigma_r}^{\circ, \bar{\xi}_{ref}}(f)(x, y)$



(c) $\kappa_{W, B}^{\circ}(f_1)(x, y)$

Figure 5.10: Example of denoising by averaging + enhancement by contrast: (a) Original noisy image $f(x, y) \in \mathbb{S}^2$ including with small targets; (b) results of denoising with the trilateral filter on the sphere (see Section 2.3.1), (c) enhancement of filtered image using the contrast) on the sphere. Note that in the Figures is shown only the image of the first coordinate on \mathbb{S}^2 .

Chapter 6

Supervised ordering on \mathbb{S}^2

When the image scenario to be analyzed includes small targets or clutter abrupt changes, the tools provided so far do not solve satisfactorily the detection of the desired targets. Fig. 6.1 provides an example of gradient on the sphere and positive top-hat on the sphere as they were described in Chapter 5. If a prior information about the data is available, it is used in the methods introduced in this chapter to accomplish the correct target detection. For this supervised approaches, a training set for each type of target and clutter are needed. The well-known hit-or-miss transform and a supervised approach for the top-hat are developed for images valued on \mathbb{S}^2 .

6.1 Complete lattices in \mathbb{S}^2

A partially ordered set (\mathcal{L}, \leq) is a complete lattice if every subset $\mathcal{A} \subset \mathcal{L}$ has both a greatest lower bound (the infimum, also called the meet) and a least upper bound (the supremum, also called the join). The meet is denoted by $\bigwedge \mathcal{A}$ and the join by $\bigvee \mathcal{A}$. A nonempty set \mathcal{A} of \mathcal{L} is a chain in \mathcal{L} if \mathcal{A} is totally ordered by \leq . The largest element of \mathcal{L} is denoted \top (top) and the smallest \perp (bottom).

Let \mathcal{L} be a complete lattice and R a nonempty set. Furthermore, let $h : R \rightarrow \mathcal{L}$ be a surjective mapping. We define a relation on R as follows

$$r \leq_h r' \iff h(r) \leq h(r'), \quad r, r' \in R$$

It is apparent that this relation \leq_h preserves reflexivity ($r \leq_h r$) and transitivity ($r_1 \leq_h r_2$ and $r_2 \leq_h r_3$ implies that $r_1 \leq_h r_3$). However, \leq_h is not a partial ordering because $r \leq_h r'$ and $r' \leq_h r$ implies only that $r =_h r'$ but not $r = r'$. This relation defines an *h-ordering*, as it was described in [10].

Using the classical taxonomy of orderings, an h-ordering is a reduced ordering.

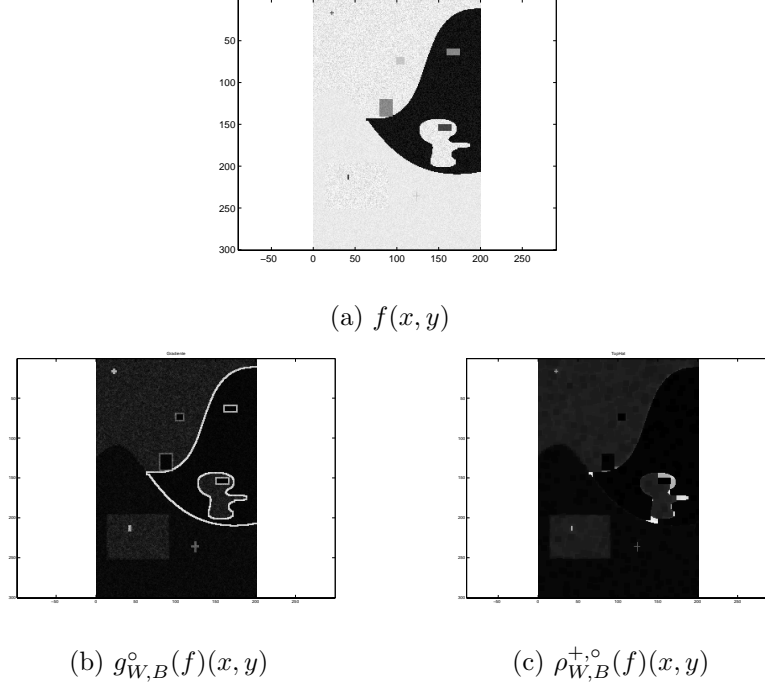


Figure 6.1: Original image (a) (first coordinate on \mathbb{S}^2) and its gradient on the sphere (b) and top-hat transformation on the sphere. False target detections are introduced. Note that the result of the gradient and the top-hat correspond are scalar images.

6.1.1 h -supervised orderings on \mathbb{S}^2

For image processing on the sphere \mathbb{S}^2 , it is necessary to define a bijective mapping h that establishes a complete lattice structure on set \mathcal{L} , i.e.,

$$h : \mathbb{S}^2 \rightarrow \mathcal{L}$$

where typically, \mathcal{L} can be identified as the real values set. Once an ordering is determined for a set $R \subset \mathbb{S}^2$, morphological processing can be directly performed.

The notion of *h-supervised ordering* was recently introduced in [27]. Let us particularize this approach to the case of \mathbb{S}^2 in the context of radar polarimetric imaging, which involves the notions of target and clutter.

From a nonempty set S of values on \mathbb{S}^2 (the training set), which is composed of the subsets T and C , such that $S = T \cup C$ and $T \cap C = \emptyset$, a *h-supervised ordering from S* satisfies the conditions:

- $h(t) = \top$ if $t \in T$,
- $h(c) = \perp$ if $c \in C$.

where \top denotes the maximum element in \mathcal{L} , whilst \perp refers to the minimum element of \mathcal{L} .

Therefore, taking into account the information contained in the data, we identify

- T as the *target training set* $T \equiv \mathcal{V}_\top = \{t_i\}_{i=1}^I$, which is related to the distribution of values of the image structures we intend to detect;
- C as the *clutter training set* $C \equiv \mathcal{V}_\perp = \{c_j\}_{j=1}^J$, which sorts the corresponding background of the scenario to analyze.

Now, for any subset of values $R = \{\xi_k\}_{k=1}^N$, $\xi_k \in \mathbb{S}^2$ we define the supervised ordering mapping

$$h(\xi_k) = K(\xi_k, T) - K(\xi_k, C) \quad (6.1)$$

where the kernel $K(\cdot, \cdot) : \mathbb{S}^2 \times \{\mathbb{S}^2\} \rightarrow \mathbb{R}^+$ is a function based on distances between a point ξ_k and a set of points (training sets target or clutter). We notice that in that case $h : \mathbb{S}^2 \rightarrow \mathbb{R}$.

A first single way consists in characterizing sets of training T and C by their first order statistics (averages on the sphere): $t = \mu^\circ(T)$ and $c = \mu^\circ(C)$. Then, an useful value of the target/clutter kernels is obtained by

$$K(\xi_k, T) = e^{-\frac{d(\xi_k, t)}{\alpha}} \quad (6.2)$$

$$K(\xi_k, C) = e^{-\frac{d(\xi_k, c)}{\alpha}} \quad (6.3)$$

where $d(\xi_k, \xi)$ is the geodesic distance of \mathbb{S}^2 and α is a normalization parameter. Note that a position on the sphere ξ_k has a high value in the ordering function $h(\xi_k)$ when is located close to the target set and far from the set clutter.

When dealing with multimodal clutter, the information from the various clutters has to be included. Thus, in $K(\xi_k, C)$ the contributions of all the different clutters should be combined. The mapping has to be balanced, i.e., for monomodal target training set, its weight has to be as significant as the combination of the clutters. Otherwise, points belonging to T are drawn to the clutter and its values in the ordering function are erroneously decreased.

Let us assume P different clutters, characterized by their corresponding Fréchet means on the sphere:

$$\begin{aligned} C_1 = \mathcal{V}_\perp^1 &= \{c_j\}_{j=1}^{J_1} \longrightarrow c_1 = \mu^\circ(C_1) \\ C_2 = \mathcal{V}_\perp^2 &= \{c_j\}_{j=1}^{J_2} \longrightarrow c_2 = \mu^\circ(C_2) \\ &\vdots \\ C_P = \mathcal{V}_\perp^P &= \{c_j\}_{j=1}^{J_P} \longrightarrow c_P = \mu^\circ(C_P) \end{aligned}$$

The proposed formulations for computing the kernels are detailed below.

Combination by addition Having identified all clutter training sets and characterized them by their Fréchet mean $c_i = \mu^\circ(C_i)$. The kernel for each set is computed individually, i.e.,

$$K(\xi_k, C_i) = e^{-\frac{d(\xi_k, c_i)}{\alpha}}$$

For the whole clutter, the values from all the kernels are added up, i.e.,

$$K(\xi_k, C) = \sum_{p=1}^P K(\xi_k, C_p) \quad (6.4)$$

In order to keep the balance for the target training set, its corresponding kernel is weighted according to the number of clutter, i.e.,

$$K(\xi_k, T) = P \cdot K(\xi_k, \mathcal{V}_T) = P \cdot e^{-\frac{d(\xi_k, t)}{\alpha}} \quad (6.5)$$

Combination by distance For a given ξ_k , we compute the kernels for each training set C_i and we select the kernel with the largest value to describe the whole clutter set, i.e.,

$$K(\xi_k, C) = K(\xi_k, C_p), \text{ such that } K(\xi_k, C_p) > K(\xi_k, C_q), \forall q \neq p \quad (6.6)$$

For the position ξ_k , the chosen clutter is the more restrictive and representative. Due to the fact that the clutter C_p is the closest set to ξ_k , i.e. at minimum distance. The kernel referred in Eq. (6.2) is used for the training target set.

Combination by grouping We define a global clutter set which is the result of lumping together all C_i

$$C = C_1 \cup C_2 \cup \dots \cup C_P = \{c_j\}_{j=1}^M \text{ where } M = \sum_{p=1}^P J_p$$

The Fréchet mean of the global set C has no geometrical sense anymore: as it is located at the barycenter of C , most of the points belonging to the different original clutter sets would be far from it, and so, it would not be representative. The distance accumulated to each element of the set C is computed instead as

$$K(\xi_k, C) = \sum_{j=1}^M \frac{1}{1 + d(\xi_k, c_j)} \quad (6.7)$$

Similarly the kernel for the training set is given by

$$K(\xi_k, T) = \sum_{i=1}^I \frac{1}{1 + d(\xi_k, t_i)} \quad (6.8)$$

Remark that it is necessary that $M = I$ for a balanced mapping function.

When target is multimodal instead, the same considerations need to be done, as for both multimodal target and clutter.

6.2 Mathematical morphology in Complete Lattices

Morphological operators used in mathematical morphology lie on complete lattice theory. We extend here, some of the morphological transformations using the h-ordering above developed.

Let $f(x, y) \in \mathcal{F}(E, \mathbb{S}^2)$ be an image valued on the sphere. Using the family of h-supervised orderings introduced in previous section, the values of image $f(x, y)$ can mapped on a complete lattice space, which correspond in fact to the real values. Therefore, we can write

$$h : \mathcal{F}(E, \mathbb{S}^2) \mapsto \mathcal{F}(E, \mathbb{R})$$

and say that $h(\cdot, \cdot)$ creates a complete lattice structure for images valued on the sphere.

Given the partial ordering induced by h , denoted by \leq_h , the *supervised dilation on the sphere* and *supervised erosion on the sphere* of an image $f(x, y) \in \mathcal{F}(E, \mathcal{L})$ are obtained replacing the operators sup and inf for \vee_h and \wedge_h according to \leq_h , i.e.,

$$\delta_{h,B}(f)(x, y) = \{\vee_h [f(u, v)], (u, v) \in B(x, y)\} \quad (6.9)$$

and

$$\varepsilon_{h,B}(f)(x, y) = \{\wedge_h [f(u, v)], (u, v) \in \check{B}(x, y)\} \quad (6.10)$$

The supervised erosion $\varepsilon_{h,B}(f)$ typically contracts the structures of image f with a value on the sphere close to the training set T of foreground (usually associated to target to be detected). It also expands the regions close to the training set C of background (or clutter zones). Dually, the dilation performs an enlargement of the structures located near foreground and dwarfs the corresponding pre-defined background.

All the other morphological operators, defined as products of dilations and erosions are generalized to the supervised framework of \mathbb{S}^2 .

6.3 Hit-or-miss transform

In mathematical morphology, hit-or-miss transform (HMT) is an operation that detects a given configuration or pattern in a binary image, using the morphological erosion operator and a pair of disjoint structuring elements. The result of the hit-or-miss transform is the set of positions, where the first structuring element has to match in the foreground, while the second structuring element has to match the background.

Let us denote $S_1 \subset E$, $S_2 \subset E$ the pair of SEs, where $S_1 \cap S_2 = \emptyset$. Then we look for all the positions where S_1 fits within a binary image I and S_2 within its complement image I^c . That can be formulated in terms of the morphological erosion, i.e.,

$$HMT(I; S_1, S_2) = \varepsilon_{S_1}(I) \cap \varepsilon_{S_2}(I^c) \quad (6.11)$$

6.3.1 Supervised hit-or-miss transformation in \mathbb{S}^2

Let us generalize the hit-or-miss transformation to images valued on the sphere. It can be used to point out and to extract those structures on an image $f(x, y) \in \mathcal{F}(E, \mathbb{S}^2)$ with a prior known shape and placed on a specific location on the sphere surface.

For the HMT, the first structuring element has to match in the foreground. Once we have established the h-supervised ordering for the pair of sets $\{T, C\}$, the supervised erosion associated to S_1 is directly computed. Whereas matching the background, we induce an inverse ordering by interchanging the sets \mathcal{V}_\top by \mathcal{V}_\perp , i.e., $\{T, C\}$ is treated as $\{C, T\}$. The expression of the hit-or-miss transform on the sphere can be written as

$$HMT(f; S_1, S_2)(x, y) = \varepsilon_{h_1, S_1}(f)(x, y) \wedge \varepsilon_{h_2, S_2}(f)(x, y) \quad (6.12)$$

where

$$h_1 = h\{T, C\} | h(b) = \perp, h(t) = \top\}$$

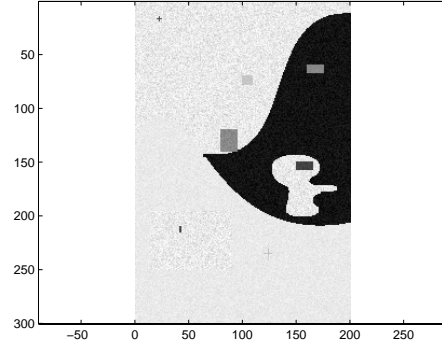
$$h_2 = h\{C, T\} | h(b) = \top, h(t) = \perp\}$$

Each structuring element S_i has a training set associated $\{S_1, T\}, \{S_2, C\}$. Thus, the formulation given in (6.12) can be generalized based on the sets of couples $\{S_i, B_i\}_{i=1, \dots, I}$, with all the SEs S_i disjoint where the B_i represent the sets of values on the sphere associated. This approach is widely explained in [28]. However, we limit here our developments on the sphere to the HMT formulation for a single pair $\{T, C\}$ and a single pair of structuring elements for the target S_1 and for the clutter S_2 . In the multimodal cases, the different sets are rather combined while defining the function h of ordering.

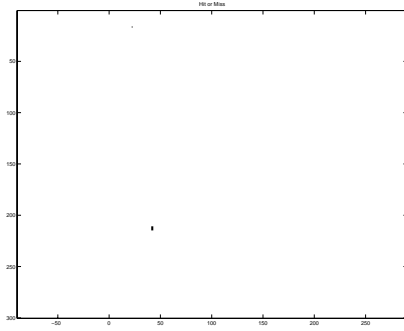
We can also include a threshold ϵ to allow a degree of noise in the detection. This parameter needs to take the same value for both erosions, meaning the mapping that defines the ordering is balanced. More precisely, it is defined by

$$HMT_\epsilon(f; S_1, S_2)(x, y) = (\varepsilon_{h_1, S_1}(f)(x, y) \wedge \varepsilon_{h_2, S_2}(f)(x, y)) < \epsilon \quad (6.13)$$

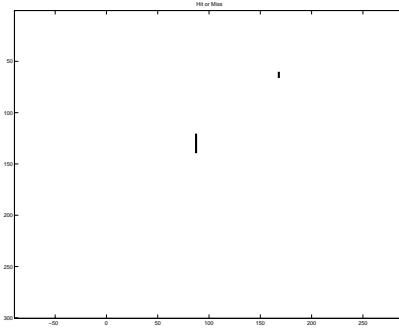
Fig. 6.2 depicts various examples of HMT_ϵ for different types of targets to be detected over different clutters. Performance of the operator for the possible combinations used in the kernel is compared in Fig. 6.3. The ROC curves evaluate the ability of the detector as a function of noise allowed, by varying the values of ϵ .



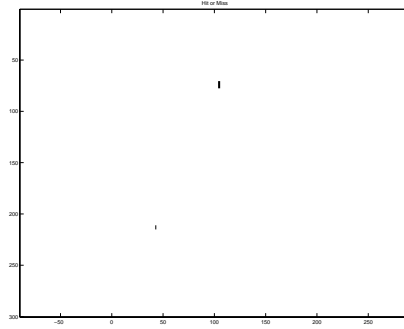
(a) $f(x, y)$



(b) $HMT(f; S_1, S_2)(x, y)$



(c) $HMT(f; S'_1, S'_2)(x, y)$



(d) $HMT(f; S''_1, S''_2)(x, y)$

Figure 6.2: (a) Original image (first coordinate on \mathbb{S}^2), (b) monomodal target and clutter case, (c) monomodal target and multimodal clutter and (d) multimodal target and monomodal clutter. The sets can be combined as defined in the *h-ordering* definition. The structuring elements are ...

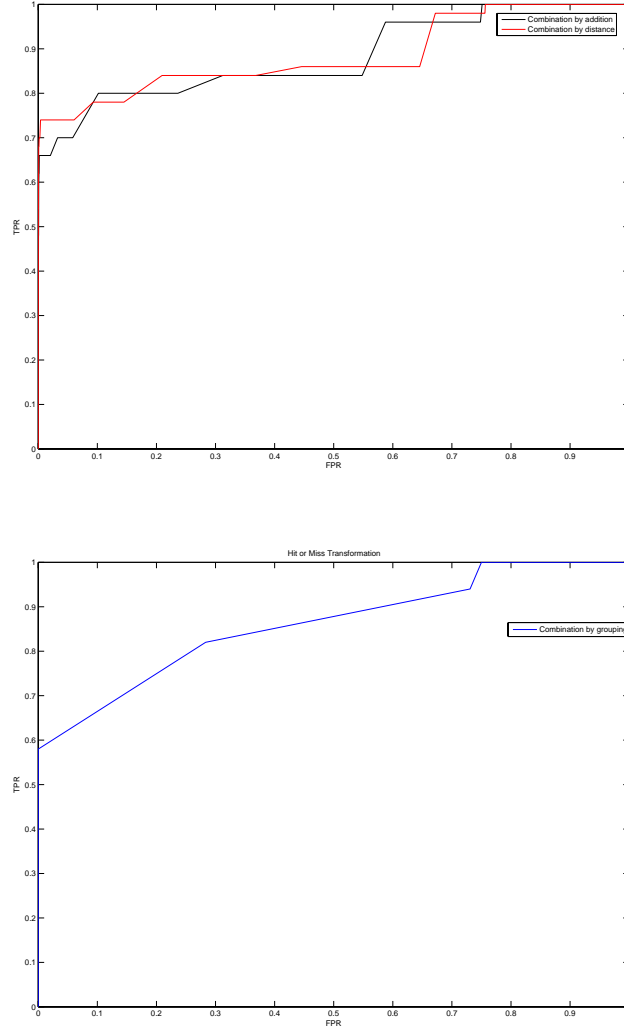


Figure 6.3: ROC curves comparing the performance of the different ordering constructions for target detection using hit-or-miss transform, obtained according to the variation of the threshold ϵ for the HMT_ϵ .

6.4 Supervised opening and supervised top-hat

A natural extension for the *supervised opening on the sphere* is defined as a supervised erosion followed by a supervised dilation

$$\gamma_{h,B}(f)(x,y) = \delta_{h,B}(\varepsilon_{h,B}(f)(x,y)) \quad (6.14)$$

Its corresponding *supervised positive top-hat on the sphere* is the residue between the original image and its supervised opening

$$\rho_{h,B}^+(f)(x,y) = d(f(x,y), \gamma_{h,B}(f)(x,y)) \quad (6.15)$$

with $d(\xi_i, \xi_j)$ the Riemannian distance on \mathbb{S}^2 .

Abrupt changes in the clutter and targets, smaller than the structuring element B and different from the ilk intended to detect, are removed when computing the opening and consequently appears in the top-hat. They introduce false positive detections, as illustrated in Fig. 6.4. A different methodology based on the decomposition of the sets in *h-supervised ordering* is proposed. Ultimately, the supervised Top-Hat proposal is detailed.

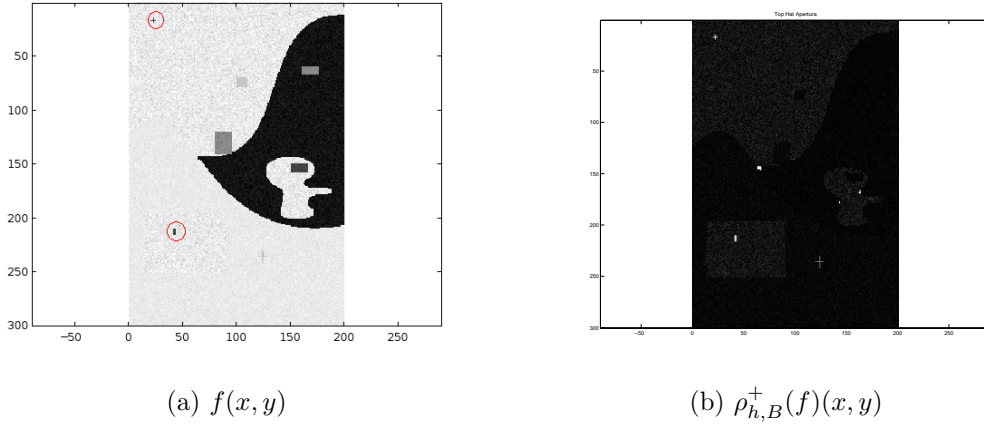


Figure 6.4: (a) Original image (first coordinate on \mathbb{S}^2), (b) positive top-Hat with the h-supervised ordering proposed. Abrupt changes in the clutter are enhanced and cross form object on the bottom right sight of the image does not correspond to the set desired targets T_K .

6.4.1 Restricted supervised top-hat in \mathbb{S}^2

Let $f(x,y) \in \mathcal{F}(E, \mathbb{S}^2)$ be an image on the sphere. Let $T_i, i = 1, \dots, I$ the target sets found in the image and $C_j, j = 1, \dots, J$ the corresponding clutter sets. Moreover, the type of

target expected to be detected conforms the particular set T_m .

Fixing T_m , marginal orderings can be defined for each pair $\{T_m, C_j\}$, $\forall j$ and $\{T_m, T_i\}$ $\forall i \neq m$. According to the analysis given in Section 6.1.1, we can formulate the ordering mappings:

$$h_i(\xi_k) = K(\xi_k, T_m) - K(\xi_k, T_i) = e^{-\frac{d(\xi_k, t_m)}{\alpha}} - e^{-\frac{d(\xi_k, t_i)}{\alpha}}$$

and

$$h_j(\xi_k) = K(\xi_k, T_m) - K(\xi_k, C_j) = e^{-\frac{d(\xi_k, t_m)}{\alpha}} - e^{-\frac{d(\xi_k, c_j)}{\alpha}}$$

with $i = 1, \dots, I$ but $i \neq m$ and $j = 1, \dots, J$. Hence, we construct every supervised opening $\gamma_{h_l, B}(f)$ according to every marginal ordering h_l , $l = 1, \dots, L$ (with $L = I + J - 1$). The difference between the original image and the supervised openings form the ensemble of marginal top-hats,

$$\rho_{h_l, B}^+(f)(x, y) = d(f(x, y), \gamma_{h_l, B}(x, y))$$

Now, we can define the *restricted supervised top-hat on the sphere* with respect to target T_m as the pixelwise minimum of all the supervised top-hats $\{\rho_{h_l, B}^+\}_{l=1}^L$:

$$\rho_{T_m, B}^+(f)(x, y) = \min_{l=1, \dots, L} \{\rho_{h_l, B}^+(f)(x, y)\} \quad (6.16)$$

False positive detections can appear in some of the marginal supervised top-hats, its value may be even higher than the value required for a target. For a structure to be hold in the restricted supervised top-hat, it has to be present in all the marginal top-hats $\rho_{h_l, B}^+$, $\forall l$ with a significant value. By choosing the minimum, the target expected takes the lower value found, and detection resolution is deteriorated. On the other hand, not desired targets and clutter changes are detected as they are not present in all $\rho_{h_l, B}^+$, $\forall l$. Fig. 6.5 illustrate an example of the performance of restricted supervised top-hat, in comparison with the marginal ones.

6.5 Conclusions and perspectives

The supervised ordering methods proposed in this chapter allow an extension formally correct of the mathematical morphology on images valued on \mathbb{S}^2 . As described above, it is required a strong a priori knowledge about the kinds of values in the image. If this training set is available, the associated operators may be extremely accurate in the target detection.

Since in many practical applications a priori information is limited, it would be interesting in continuing this work, conceiving new strategies of ordering for the data lying on the sphere. Strategies capable to automatically determine the kinds of targets, clutters in the image. For example, clustering algorithms on the sphere (e.g. k-means) or statistical modeling of distributions (e.g. E-M algorithm) are lines that might be considered.

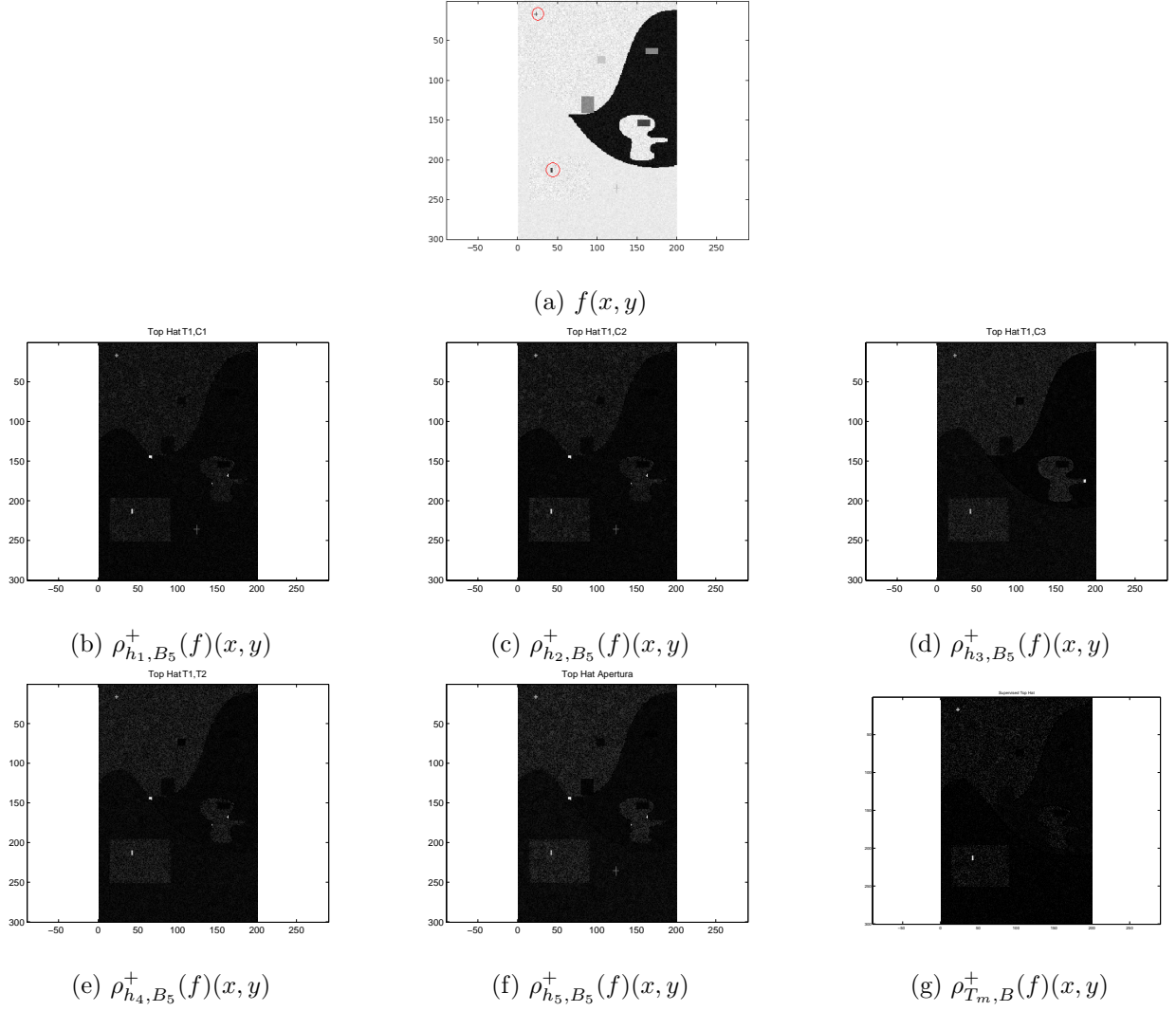


Figure 6.5: (a) Original image (first coordinate on \mathbb{S}^2), all marginal supervised top-hats (b)(c)(d)(e)(f) and the minimum pixel to pixel for all of them leads to the restricted supervised top-hat (g).

Chapter 7

Conclusions and perspectives

The main goal of this project is to survey the generalization of mathematical morphology to images valued on the unit sphere and develop some improved techniques for target detection. In this chapter a conclusion is given based on the analysis performed followed by additional guidelines for future work.

7.1 Main contributions

This reserach has contributed to image processing when data set is embedded on the sphere surface. Various filtering methods are described according to the configuration of the data. The performance of the different techniques are compared and its suitability for denoising issues is discussed. We propose an extension for classical gradient and top-hat for data distributed on the unit sphere, and evaluate their response for target detection purposes. The need for a partial ordering on \mathbb{S}^2 has a particular interst for the generalization of all morphological operators. We introduce an approach to dispose local supremum and infimum, which allows to define the (pseudo-) dilation/erosion on the sphere. Other tools commonly used to identify structures on an image emerge from this new approach, such as opening/closing, gradient and top-hat, or contrast operators for enhancing contours. Finally, supervised orderings on \mathbb{S}^2 are explored. The different proposals for the ordering computation are analyzed and compared. These orderings may ultimately provide a generalization of all morphological operators on the sphere. Supervised hit-or-miss and supervised top-hat are detailed for its particular pertinence in target detection.

From the analysis performed, it can be concluded that mathematical morphology proffers a wide variety of tools appropriate for target detection issues. Its extension to \mathbb{S}^2 presents a challenging topic to be subject to further studies.

7.2 Future work

The different methods exposed in this project require of a validation on real polarimetric data. The interest of this operators for the treatment of other images valued on the sphere might be studied. As for the mentioned orientation-valued images, 3D images of vector gradient and HARDI medical images.

The scenario would be different if data were located inside the sphere instead. Morphological operators restricted to the variability of the radius may be explored. Thus, the data would be represented as a four components vector. Different methods of averaging quaternions can be considered for denoising purposes.

An extensive analysis, when other spaces of representation are used, could be done. The definition of the supremum and infimum in the space associated to stereographic projection and to the Poincaré disk.

Moreover, including the Doppler information contained in the data may reveal new interesting approaches.

If there were a formulation of quantum mathematical morphology, the state of every pixel would be a linear combination of the pure states of the system. Similarly as we described for the Poincaré sphere, in quantum mechanics the geometrical model corresponds to the Bloch sphere. And its model in physics is associated to the space of a two-level quantum mechanical system, called *qubit*. The extension of morphology operators on the sphere to quantum mechanics remains to further studies which are out of the scope of this project.

Bibliography

- [1] J. Astola, P. Haavisto, Y. Nuevo. Vector Median Filters. *Proc. of the IEEE*, 78(4) : 678–689, 1990.
- [2] R. Bhattacharya, V. Patrangenaru. Large Sample Theory of Intrinsic and Extrinsic Sample Means on Manifolds - II. *The Annals of Statistics*, 33(3): 1225–1259, 2005.
- [3] M. Black, A. Rangarajan. On the unification of line processes, outlier rejection, and robust statistics with applications in early vision. *Int. J. Comput. Vis.*, 19 :57–92, 1996.
- [4] S.R. Buss, J.P. Fillmore. Spherical averages and applications to spherical splines and interpolation. *ACM Transactions on Graphics*, 20: 95–126, 2001.
- [5] F. Catte, P.-L. Lions, J.-M. Morel, T. Coll. Image selective smoothing and edge detection by nonlinear diffusion. *SIAM Journal on Numerical Analysis*, 29(1):182–193: 1992.
- [6] M. Elad. On the Origin of the Bilateral Filter and Ways to Improve It. *IEEE Trans. on Image Processing*, 11(10):1141–1151, 2002.
- [7] S. Fiori. On vector averaging over the unit hypersphere. *Digital Signal Processing*, 19:715–725, 2009.
- [8] P.T. Fletcher, S. Venkatasubramanian, S. Joshi. Robust Statistics on Riemannian Manifolds via the Geometric Median. In *Proceedings of CVPR’08*, 2008.
- [9] M. Fréchet. Les éléments aléatoires de nature quelconque dans un espace distancié. *Ann. Inst. H. Poincaré*, 10: 215–310, 1948.
- [10] J. Goutsias, H.J. A.M. Heijmans and K. Sivakumar, Morphological operators for image sequences, *Computer Vision and Image Understanding* **62** (1995), pp. 326–346
- [11] A. Hanbury, J. Serra. Morphological Operators on the Unit Circle. *IEEE Transactions on Image Processing*, 10(12):1842–1850, 2001.
- [12] H. Heijmans, C. Ronse. The Algebraic Basis of Mathematical Morphology. Part I: Dilations and Erosions. *CVGIP: Image Understanding*, 50(3):245–295, 1990.

-
- [13] H. Karcher. Riemann center of mass and mollifier smoothing. *Communications on Pure and Applied Mathematics*, 30: 509–541, 1997.
 - [14] H. Kramer, J. Bruckner. Iterations of non-linear transformations for enhancement on digital images. *Pattern Recognition*, Vol. 7, 53–58, 1975.
 - [15] R.L. Lagendijk, J. Biemond, D.E. Boeke. Regularized iterative image restoration with ringing reduction. *IEEE Trans. Acoust., Speech, Signal Processing*, 36: 1874–1887, 1988.
 - [16] J.S. Lee, E. Pottier. Polarimetric radar imaging: from basics to applications. CRC Press, Taylor and Francis, 2009
 - [17] S. Paris, P. Kornprobst, J. Tumblin, F. Durand. Bilateral Filtering: Theory and Applications. *Foundations and Trends in Computer Graphics and Vision*, 4(1):1–73, 2008.
 - [18] X. Pennec. Intrinsic statistics on Riemannian manifolds: basic tools for geometric measurements. *Journal of Mathematical Imaging and Vision*, 25(1), 2006.
 - [19] P. Perona, J. Malik. Scale-Space and Edge Detection Using Anisotropic Diffusion. *IEEE Trans. Pattern Anal. Mach. Intell.*, 12(7): 629–639, 1990.
 - [20] J. Roerdink. Adaptivity and group invariance in mathematical morphology. In *Proc. of IEEE International Conference on Image Processing (ICIP'09)*, pp. 2253–2256, 2009.
 - [21] J. Serra. *Image Analysis and Mathematical Morphology, Vol I*. Academic Press, NY, London, 1982.
 - [22] J. Serra. *Image Analysis and Mathematical Morphology Vol.2: Theoretical Advances*. Academic Press, NY, London, 1988.
 - [23] J. Serra. Toggle mappings. In (Simon, Ed.) *From Pixels to Features*, North Holland, Amsterdam, pp. 61–72, 1989.
 - [24] N. Sochen, R. Kimmel, and A. M. Bruckstein. Diffusions and confusions in signal and image processing. *J. Math. Imag. Vis.*, 14(3):195–209, 2001.
 - [25] P. Soille. *Morphological Image Analysis*. Springer-Verlag, Berlin, 1999.
 - [26] C. Tomasi, R. Manduchi. Bilateral filtering for gray and color images. In *Proc. of 6th Int. Conf. Computer Vision (ICCV'98)*, 839–846, New Delhi, India, 1998.
 - [27] S. Velasco-Forero, J. Angulo. Morphological processing of hyperspectral images using kriging-based supervised ordering. In *ICIP(2010)* 1409-1412
 - [28] S. Velasco-Forero, J. Angulo. Hit-or-Miss Transform in Multivariate Images. In *Proceedings of ACIVS (1)'2010*. pp.452 463

- [29] Y. Wang, C. Han. PolSAR Image Segmentation by Mean Shift Clustering in the Tensor Space. In *Acta Automatica Sinica* 36: 798–806, 2010.
- [30] J. Weickert. *Anisotropic Diffusion in Image Processing*, ECMI Series, Teubner-Verlag, Stuttgart, Germany, 1998.
- [31] L. Yaroslavsky. *Digital Picture Processing, An Introduction*. Springer Verlag, Berlin, Heidelberg, 1985.
- [32] J.Zallat, C. Heinrich. Polarimetric data reduction: a Bayesian approach. *Optics Express*, Vol. 15, Issue 1, pp. 83-96 (2007)

List of Figures

1.1	Polarization ellipse.	17
1.2	(a) Stokes parameters and latitude/longitude on the sphere. (b) Polarization states on the Poincaré sphere.	21
1.3	Simulated image, valued on the sphere $f(x, y) \in \mathcal{F}(E, \mathbb{S}^2)$ and used to illustrate the proposed methods: (a) (b) and (c) show the value of each of the coordinates in \mathbb{R}^2 . While their situation on \mathbb{S}^2 and the corresponding polarization states are displayed in (d).	24
1.4	Image valued on \mathbb{S}^2 with a higher degree of noise.	25
1.5	Image valued on \mathbb{S}^2 that shows a more complex scenario with several types of targets and clutters.	26
2.1	The two sets show different distributions on \mathbb{S}^2 . In yellow, the median value and in green, the mean, which is located inside the sphere.	29
2.2	Iterative method for computing the Fréchet mean for data on the sphere: (a) All the points are projected onto the plane tangent (b) at the starting point \mathbf{y}_t (c) an expectation is calculated on the tangent space and the result is projected back onto the sphere.	31
2.3	Fréchet mean for two sets with different distributions of point on \mathbb{S}^2 . In black the starting point, different colors points correspond to the consecutive iterations until the algorithm converges to the yellow point.	33
2.4	Noisy images and the output of filtering using the Fréchet mean: (a) and (c) original images, (b) and (d) filtered images. The window B is a square of size 5×5 pixels.	34
2.5	Original image (a) and comparison between mean filtering by regular Fréchet mean (b) and by Weighted Fréchet mean with weights in the pixels space $E(c)$. In both cases B is a square of size 5×5 pixels and $\sigma = 0.9$	36
2.6	Noise reduction of original image (a) using the bilateral filter (b), with parameters $\sigma_s = 0.9$ and $\sigma_i = 0.9$ in a window B of size 5×5 pixels.	37

2.7	When the targets to be detected are small in the original image (a), the tri-lateral filter adapted to this particular targets achieves better performance (c) than bilateral filter (b).	39
4.1	Original images (a),(e),(i), (first coordinate on \mathbb{S}^2). Morphological gradient for three different noise levels $\sigma = 0.1, \sigma = 0.3$ and $\sigma = 1$, with B a square of size 3×3	45
4.2	<i>Self-complementary Top-Hat</i> for three different sizes of the structuring element B.	47
4.3	ROC curves representing the performance of the gradient for different noise levels. For $\sigma = 1$ the different filters results are compared.	51
5.1	Figure (a) shows the original set R , and its Fréchet mean in green. Figure (b) is the result of the rotation of the set to \mathbf{N} . Figure (c) illustrates how $\vec{\nu}_{sup}$ is projected back to the sphere and the rotation is reversed, in yellow the value of the supremum.	54
5.2	Tangent plane $T_{\mathbf{N}}\mathbb{S}^2$, with all the projected points $\vec{\nu}_i$. We note that $\tilde{\xi}$, in green, is found at the origin. The red dots are the four candidates $\vec{\nu}_j^\square$, $j = 1, \dots, 4$, and the yellow one is the furthest from the origin $\vec{\nu}_{sup}$	55
5.3	Inverted plane from tangent plane $T_{\mathbf{N}}\mathbb{S}^2$. The points are displayed once their coordinates have been inverted, $\vec{\theta}_i$, $\tilde{\xi}$ in green is found at the origin (without inversion since its inversion correspond to the infinity). The four red dots are the candidates to infimum and in yellow, the chosen one.	56
5.4	Tangent plane $T_{\mathbf{N}}\mathbb{S}^2$. The four red dots are the four candidates for the supremum $\vec{\nu}_j^\square$, $j = 1, \dots, 4$, and the yellow is the furthest from the origin $\vec{\nu}_{sup}$. While the four dots in pink are the candidates for the infimum, obtained by inversion of $\vec{\theta}_j^\square$, $j = 1, \dots, 4$, and the black is the closest to the Fréchet mean $\vec{\nu}_{inf}$	57
5.5	Computation of infimum for a set of points, including the result of projecting back to the sphere and undoing the rotation. In yellow the value of the infimum.	58
5.6	Case of computation of the infimum where the coordinates can not be inverted.	58
5.7	Examples of pseudo-dilation $\delta_{W,B_n}^\circ(f)(x,y)$ and pseudo-erosion $\varepsilon_{W,B_n}^\circ(f)(x,y)$ of image $f(x,y) \in \mathbb{S}^2$ in (a). The structuring element B_n is a square of size $n \times n$ pixels and W is a square of size \times . Note that in the Figures is shown only the image of the first coordinate on \mathbb{S}^2	61
5.8	Examples of gradient $g_{W,B_n}^\circ(f)(x,y)$ of image $f(x,y) \in \mathbb{S}^2$. The image of the first coordinate on \mathbb{S}^2 of original image is given in (a). Note that the result of the gradient correspond to the scalar image given in (b) and (c).	63

5.9	Examples of pseudo-opening $\gamma_{W,B_n}^\circ(f)(x,y)$ of image $f(x,y) \in \mathbb{S}^2$, given in (a), and its residue (top-hat) $\rho_{W,B_n}^{+,\circ}(f)(x,y)$. The structuring element B_n is a square of size $n \times n$ pixels and W is a square of size \times . Note that in the Figures (a)-(d) is shown only the image of the first coordinate on \mathbb{S}^2 , however for top-hat images, the result is the given scalar image.	66
5.10	Example of denoising by averaging + enhancement by contrast: (a) Original noisy image $f(x,y) \in \mathbb{S}^2$ including with small targets; (b) results of denoising with the trilateral filter on the sphere (see Section 2.3.1), (c) enhancement of filtered image using the contrast) on the sphere. Note that in the Figures is shown only the image of the first coordinate on \mathbb{S}^2	67
6.1	Original image (a) (first coordinate on \mathbb{S}^2) and its gradient on the sphere (b) and top-hat transformation on the sphere. False target detections are introduced. Note that the result of the gradient and the top-hat correspond are scalar images.	69
6.2	(a) Original image (first coordinate on \mathbb{S}^2), (b) monomodal target and clutter case, (c) monomodal target and multimodal clutter and (d) multimodal target and monomodal clutter. The sets can be combined as defined in the <i>h-ordering</i> definition. The structuring elements are	74
6.3	ROC curves comparing the performance of the different ordering constructions for target detection using hit-or-miss transform, obtained according to the variation of the threshold ϵ for the HMT_ϵ	75
6.4	(a) Original image (first coordinate on \mathbb{S}^2), (b) positive top-Hat with the h-supervised ordering proposed. Abrupt changes in the clutter are enhanced and cross form object on the bottom right sight of the image does not correspond to the set desired targets T_K	76
6.5	(a) Original image (first coordinate on \mathbb{S}^2), all marginal supervised top-hats (b)(c)(d)(e)(f) and the minimum pixel to pixel for all of them leads to the restricted supervised top-hat (g).	78